JGR Solid Earth

Key Points:

- We present a new method for modeling geometrically complex ruptures in heterogeneous media using distributed point sources
- Postseismic deformation is best explained by models that include a deep shear zone below the earthquake rupture
- Up to ~0.2 m of shallow afterslip occurred within 1 year after the earthquake, insufficient to compensate for the coseismic shallow slip deficit

Author Contributions:

Conceptualization: Zeyu Jin, Yuri Fialko
Data curation: Hongfeng Yang, Yu Li
Formal analysis: Zeyu Jin
Funding acquisition: Yuri Fialko, Yu Li
Methodology: Zeyu Jin
Software: Zeyu Jin
Supervision: Yuri Fialko
Visualization: Zeyu Jin
Writing – original draft: Zeyu Jin
Writing – review & editing: Zeyu Jin, Yuri Fialko, Hongfeng Yang, Yu Li

Transient Deformation Excited by the 2021 M7.4 Maduo (China) Earthquake: Evidence of a Deep Shear Zone

Zeyu Jin[1] [ID]**, Yuri Fialko[1]** [ID]**, Hongfeng Yang[2]** [ID]**, and Yu Li[3]**

[1]Institute of Geophysics and Planetary Physics, Scripps Institution of Oceanography, University of California San Diego, La Jolla, CA, USA, [2]Earth System Science Programme, The Chinese University of Hong Kong, Hong Kong, China, [3]China Earthquake Networks Center, China Earthquake Administration, Beijing, China

Abstract We use Sentinel-1 and ALOS-2 Interferometric Synthetic Aperture Radar (InSAR), and Global Navigation Satellite System (GNSS) data to investigate the mechanisms of coseismic and postseismic deformation due to the 2021 M7.4 Maduo (China) earthquake. We present a refined coseismic slip model constrained by the rupture trace and precisely located aftershocks. The InSAR time series corrected for the atmospheric and decorrelation noise reveal postseismic line of sight displacements up to ~0.1 m. The displacements are discontinuous along the fault trace, indicating shallow afterslip and velocity-strengthening friction in the top 2–3 km of the upper crust. The magnitude of shallow afterslip is however insufficient to compensate for the coseismic slip deficit, implying substantial off-fault yielding. The observed surface deformation does not exhibit obvious features that could be attributed to poroelastic effects. We developed a fully coupled model that accounts for both stress-driven creep on a deep localized shear zone and viscoelastic relaxation in the bulk of the lower crust. The mid- to near-field data can be reasonably well explained by deep afterslip and/or non-Maxwellian visco-elasticity. Our results suggest a power-law stress exponent of ~4–4.5 assuming a power-law rheology, and transient and steady-state viscosities of 10^{18} and 10^{19} Pa s, respectively, assuming a bi-viscous (Burgers) rheology. However, a good fit to the GNSS data cannot be achieved assuming the bulk viscoelastic relaxation alone, and requires a contribution of deep afterslip and/or a localized shear zone extending through much of the lower crust.

Plain Language Summary A large earthquake occurred in the north-east Tibetan Plateau (Qinghai Province, China) on 21 May 2021. We use data collected by orbiting satellites to measure subtle (millimeter to centimeter-scale) displacements of the Earth's surface that occurred in 1 year following the Maduo earthquake. The observed rates and spatial patterns of surface displacements are used to infer the mechanisms of stress relaxation and mechanical properties of rocks at depth. We find evidence of continued slip on the fault that produced the Maduo earthquake, both near the surface, and below the seismogenic zone. Our results suggest that major faults that cut through the Tibetan Plateau are associated with deep roots that extend into the lower crust. The observed shallow slip is insufficient to compensate for the near-surface slip deficit that accrued during the earthquake. This suggests that some amount of the near-surface coseismic shear was distributed over a wider zone around the earthquake rupture.

1. Introduction

The M_w7.4 Maduo earthquake occurred on 21 May 2021 in the north-eastern part of the Tibetan Plateau (Figure 1). Field mapping, space geodetic imaging, and aftershock data indicate that the earthquake ruptured a ~170 km-long left-lateral strike-slip fault (e.g., Jin & Fialko, 2021; W. Wang et al., 2021; D. Zhao et al., 2021b). The earthquake rupture is located within the Bayan Har Block, which is bounded by the Kunlun fault in the north and Xianshuihe fault system in the south, two major left-lateral faults accommodating the eastward extrusion of the Tibetan Plateau (e.g., Tapponnier et al., 1982; Thatcher, 2007). Both the Kunlun and Xianshuihe fault systems produced major earthquakes in the last century, including the 2001 M_w7.9 Kokoxilli earthquake that occurred on the main Kunlun fault, the 1997 M_w7.6 Manyi earthquakes that occurred on a western end of the Kunlun fault system, and the 2010 M_w7.1 Yushu and the 2022 M_w6.6 earthquakes that occurred on the Yushu-Garzi-Xianshuihe fault system (e.g., Y. An et al., 2022; Bai et al., 2018; Funning et al., 2007; Klinger et al., 2005; Xiong et al., 2010). This remarkable sequence of large earthquakes provides an excellent opportunity to probe the rheological structure of the Tibetan lithosphere.
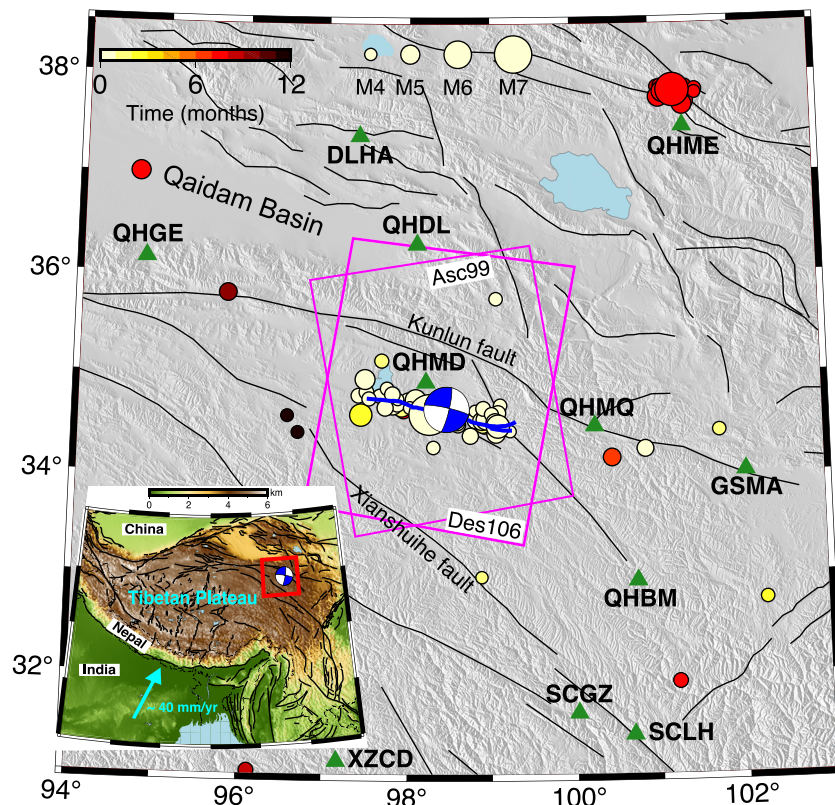
Figure 1. Tectonic setting of the 2021 M7.4 Maduo earthquake. Blue curvy line denotes the rupture trace mapped using the Sentinel-1 range offsets (Jin & Fialko, 2021). White-and-blue "beach ball" denotes the centroid location and the focal mechanism from the Global CMT catalog. Thin black lines denote active faults (Taylor & Yin, 2009). Color circles denote shallow (hypocenter depth less than 30 km) aftershocks over 1 year following the mainshock. Magenta rectangles denote swaths of Sentinel-1 SAR data used in this study. Green triangles denote continuous Global Navigation Satellite System sites used in this study. (Inset) Topography and fault map of the India-Eurasia collision zone.

Previous studies suggested that the mid to lower crust beneath the Tibetan Plateau may be warm and mechanically weak, possibly due to a presence of partial melt. Relevant geophysical observations include high electric conductivity (e.g., Unsworth, 2010; Unsworth et al., 2004; W. Wei et al., 2001), low seismic velocities in the lower crust and upper mantle (e.g., McNamara et al., 1997; Ni & Barazangi, 1983), and high seismic attenuation (e.g., Fan & Lay, 2003; Rodgers & Schwartz, 1998). A weak lower crust was proposed to explain the uplift (Burov & Watts, 2006; W.-L. Zhao & Morgan, 1987) and outward expansion (Clark & Royden, 2000) of the Tibetan Plateau, with some models implying a long-term effective viscosity of the lower crust of less than 10^{17} Pa s (Royden et al., 1997).

Studies of postseismic response due to large earthquakes however suggest much higher viscosities that furthermore appear to increase with time following the event. For example, Liu et al. (2019) estimated viscosity of the lower crust beneath the Songpan-Ganzi terrane to be $2–3 \times 10^{18}$ Pa s in the first year following the 2001 Kokoxilli earthquake, increasing by an order of magnitude in the subsequent 15 years. D. Zhao et al. (2021a) inferred a bi-viscous (Burgers) rheology with the transient and steady-state viscosities of the lower crust of 5×10^{18} and 4×10^{19} Pa s, respectively. Comparable, if not higher, viscosities were estimated by studies of postseismic transients at the plateau margins (Huang et al., 2014; Jin et al., 2022; K. Wang & Fialko, 2014, 2018; M. Wang et al., 2021). Previous work also showed that inferences of the effective viscosity of a ductile substrate may be complicated in the presence of multiple relaxation mechanisms (e.g., Fialko, 2004a; Rousset et al., 2012; Takeuchi & Fialko, 2013; D. Zhao et al., 2021a). In particular, a localized shear on deep fault roots may bias estimates of the bulk rheologic properties of ambient rocks if the former is not taken into account (Takeuchi & Fialko, 2012; K. Wang & Fialko, 2018; Wright et al., 2013; D. Zhao et al., 2021a). Therefore, a rigorous assessment of multiple mechanisms that may potentially contribute to the observed deformation transients is needed for robust estimates of in situ material properties below the brittle-ductile transition.

An important starting point in studies of postseismic deformation is an accurate and well-constrained model of coseismic slip. Published coseismic models of the Maduo earthquake are mostly based on solutions for rectangular dislocations in a homogeneous or layered elastic half-space (e.g., Jin & Fialko, 2021; Yue et al., 2022; D. Zhao et al., 2021b). While such models do allow for some complexity in the rupture geometry, high quality observations including space geodetic imaging and precisely relocated aftershocks (He et al., 2022; W. Wang et al., 2021) warrant more detailed models that include spatial variations in the fault attitude, as well as mechanical properties of the host rocks.

In this study, we first refine a coseismic slip model using a new representation based on a superposition of point sources that honors the geometrically complex fault trace and the aftershock distribution, resulting in a non-planar slip interface that varies along both strike and dip directions. We then present the Interferometric Synthetic Aperture Radar (InSAR) and Global Navigation Satellite System (GNSS) observations of postseismic deformation over ∼1 year following the Maduo earthquake. We compare the observed postseismic deformation to models that assume various time-dependent relaxation mechanisms, including afterslip, viscoelastic, and poroelastic deformation, and place constraints on the effective mechanical properties of rocks comprising continental lithosphere in the northeast Tibetan Plateau.

2. Kinematically Consistent Models of Coseismic Slip on Non-Planar Faults

A common approach in modeling earthquake ruptures is to approximate the latter by a superposition of rectangular dislocations (e.g., Fialko, 2004b; Freymueller et al., 1994; Hsu et al., 2009). However, in case of curved or multi-segment faults the use of rectangular dislocations typically gives rise to gaps, overlaps, tears, and other unphysical discontinuities between the modeled sub-faults (e.g., Hamling et al., 2017; Jin & Fialko, 2020; Tong et al., 2010). Triangular dislocations offer a greater flexibility at discretizing complex fault geometries, but analytic solutions are limited to homogeneous elastic media (Barnhart & Lohman, 2010; Meade, 2007; Thomas, 1993). At the same time, semi-analytic or numerical solutions for point sources are readily available in case of layered as well as fully heterogeneous elastic media (e.g., Barbot, Fialko, & Sandwell, 2009; R. Wang et al., 2003; L. Zhu & Rivera, 2002). Because finite dislocations can be approximated by a sufficiently dense distribution of point sources (e.g., Barbot & Fialko, 2010a, 2010b; R. Wang et al., 2003), we developed a method based on a superposition of point sources in a heterogeneous medium to represent slip on arbitrarily shaped fault surfaces.

Following the approach of Jin and Fialko (2020), we make use of the rupture trace and precisely located aftershocks to constrain the subsurface rupture geometry. We fit a smooth curved surface that attempts to honor the rupture trace as close as possible, and aftershock locations in the least squares sense (Figure 2). We then tessellate the inferred rupture surface into a "watertight" mesh of finite slip patches. Here we use a triangular tessellation for simplicity, but the geometry of slip patches in general can be arbitrary, defined for example, by Voronoi cells (Dettmer et al., 2014; Voronoi, 1908). A desirable quality of the discretized model is that slip patches are as small as necessary to fit the data, but as large as needed to be well resolved—that is, the model resolution matrix is as close as possible to the identity matrix (e.g., M. An, 2012; Backus & Gilbert, 1968; Fialko, 2004b; Lohman & Simons, 2005). In case of sub-vertical strike-slip faults, this can be achieved by increasing the size of individual slip patches (model resolution cells) with depth in a geometric progression (Fialko, 2004b; Simons et al., 2002). In our model the size of triangular elements increases from ∼2.5 at the Earth's surface to ∼10 km at the bottom of the fault model at depth of 20 km.

Each triangular dislocation element (TDE) is then represented by a superposition of point sources that are uniformly distributed inside the element. To ensure the accuracy of point source representation of the TDEs, we performed synthetic tests in which we compared predictions of our model in case of a homogeneous uniform elastic half-space to the available analytical solutions. The synthetic tests assumed a unit slip along either strike or dip direction on a TDE having a characteristic dimension of ∼8 km, and a centroid depth of ∼9 km (Figure S1 in Supporting Information S1). Figure S2 in Supporting Information S1 shows that the numerical errors due to a point source approximation are less than 3% provided that the element edges are resolved by more than 16 point sources. Figure S3 in Supporting Information S1 shows that the numerical error gradually decreases as the element depth increases, indicating that fewer points are necessary to adequately represent sources which size is small compared to their depth (Fialko, Khazan, & Simons, 2001; Toupin, 1965).

The errors are highest for the elements that intersect the Earth's surface. To ensure a sufficient accuracy, we used a spatial interval of 100 m (smaller than the data sampling interval) between point sources that populate the shallowest TDEs. For elements at greater depth, the spacing between point sources increases proportionally to the element depth, following the same geometric progression as for the element dimensions. The resulting numerical
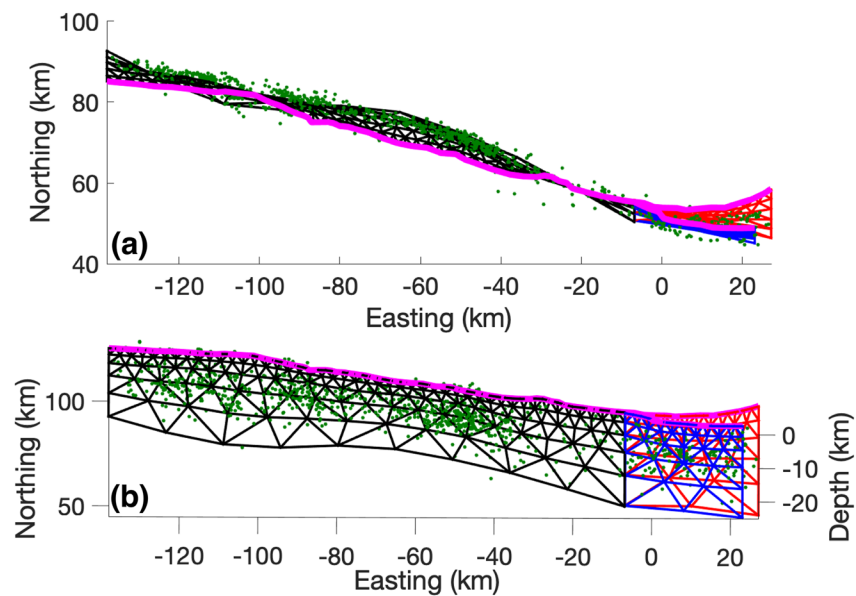
Figure 2. (a) Top and (b) side views of a non-planar fault surface determined using rupture trace (magenta lines) and relocated aftershock data (dark green dots) using a weighted least squares method. Each curved surface is tessellated using triangles which size increases with depth. The black mesh corresponds to the main earthquake rupture, and the red and blue meshes correspond to two sub-parallel faults at the east end of the earthquake rupture.

errors of all TDEs are less than 1%. The Green's functions for each TDE were computed by adding the Green's functions from all point sources inside the respective element. The attitude of point sources (i.e., strike and dip angles) follows the plane of a TDE they belong to, but in case of highly curved faults could instead follow the local attitude of a tessellated curved surface. The Green's functions are computed for a unit slip on a TDE in the strike and dip directions, for all observation points at the free surface. We then set up a linear inversion subject to a positivity constraint, regularization, and boundary conditions as described in Jin and Fialko (2020). The data used in the coseismic slip inversion include the line of sight (LOS) displacements and range offsets from the ascending and descending tracks of Sentinel-1 satellites (Jin & Fialko, 2021) complemented by ALOS-2 interferogram from a descending track 42 that provides a better near-field coverage due to a longer radar wavelength (Figure S4 in Supporting Information S1). Figure 3 shows a comparison of coseismic slip models derived using (a) rectangular dislocations in a homogeneous elastic half-space, (b) triangular dislocations in a homogeneous elastic half-space, (c) point source approximation of TDEs in a homogeneous elastic half-space, and (d) point source approximation of TDEs in a layered elastic half-space. For the latter, we used elastic moduli from a one-dimensional (1-D) regional seismic velocity model of the north-eastern Tibetan Plateau (see Figure S4 in Jin and Fialko (2021)). A comparison of inversions using numerical and analytic models of TDEs in a homogeneous elastic half-space shows differences of less than 3% (Figures S2 and S3 in Supporting Information S1). All models are able to fit the data equally well, with the misfit reduction of InSAR data of more than 96% (Figure S4 in Supporting Information S1). The inferred slip distributions are generally quite similar between models shown in Figures 3a and 3b, in part because deviations of the rupture geometry from a sub-vertical plane are rather modest. One apparent effect of neglecting fault curvature is an underestimated depth extent of coseismic slip (cf. Figures 3a and 3c). The same holds for neglecting increases in the elastic rigidity with depth (cf. Figures 3c and 3d), as reported in earlier studies (e.g., Fialko, 2004b; Hearn & Bürgmann, 2005; Jin & Fialko, 2020). A comparison shown in Figure 3 illustrates a feasibility of our method based on a point source representation of earthquake ruptures having complex geometries.

3. Postseismic Deformation

To investigate transient deformation excited by the 2021 Maduo earthquake, we analyzed Sentinel-1 and ALOS-2 InSAR data collected over a time period of 1 year following the earthquake, as well as GNSS data from 11 continuous sites from the Chinese GNSS network located within ~400 km from the earthquake rupture (Figure 1).
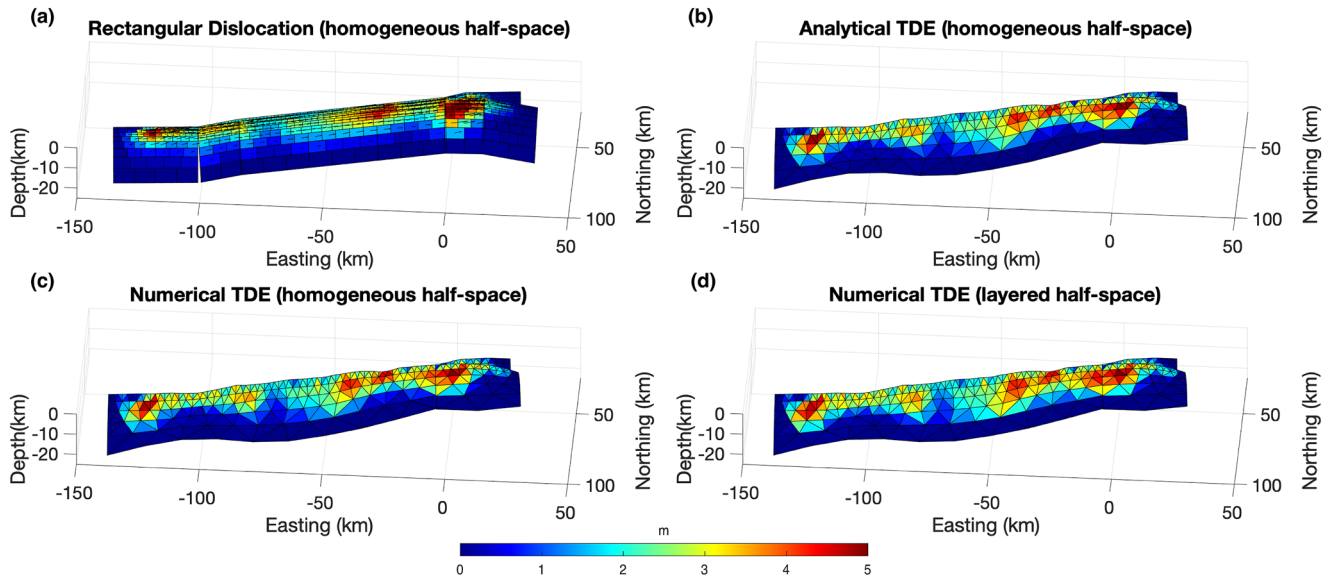
Figure 3. A comparison of coseismic slip models that use different model discretizations and material properties. (a) Rectangular dislocations, homogeneous elastic half-space. (b) Triangular dislocation elements (TDE), analytic solution, homogeneous elastic half-space. (c) TDE, point source approximation, homogeneous elastic half-space. (d) TDE, point source approximation, layered elastic half-space. Colors denote the amplitude of slip in meters.

3.1. InSAR Data

We used Sentinel-1 data collected in the TOPS mode from the ascending track 99 and descending track 106, and ALOS-2 data collected in the ScanSAR mode from the descending track 42. The data were processed using GMTSAR (Sandwell et al., 2011). The 30 m digital elevation model from the Shuttle Radar Topography Mission (Farr & Kobrick, 2000) was used to remove the radar phase due to topography. Elevation changes that might have occurred over ~20 years (e.g., Lin et al., 2006) since the Shuttle Radar Topography Mission are neglected because a tight orbital control of Sentinel-1 satellites gives rise to the ambiguity height of more than 50 m (e.g., Rosen et al., 2000, Equation 31).

InSAR data are subject to decorrelation noise in the presence of vegetation, variations in the soil moisture, etc. Spatial filtering and multilooking are commonly used to reduce the phase speckle, and facilitate phase unwrapping. However, filtering and multilooking may lead to a non-zero phase closure in circuits of interferometric pairs. The latter represent the difference between a sum of N sequential interferograms and a direct interferogram connecting the first and last acquisition dates, with the noise originating primarily from the sum of sequential interferograms (e.g., Biggs et al., 2007; De Zan et al., 2015; Lau et al., 2018). The circuit non-zero closure errors are non-random, and accumulate progressively as more interferograms are added (e.g., Tymofyeyeva et al., 2019; Zheng et al., 2022). For sufficiently large data sets, the decorrelation noise becomes a major limiting factor for measuring small-amplitude deformation.

To mitigate the systematic cumulative bias due to decorrelation noise, we apply an empirical correction that enforces phase closure in elementary circuits formed by triplets of the nearest acquisitions. This correction assumes that the respective phase errors are evenly distributed between interferograms forming each circuit. The algorithm consists in the following steps:

1. We generate a set of sequential interferograms, complemented by a set of interferograms that connect every other acquisition date ("skip 1" set). For example, given an acquisition date i, the sequential interferograms are $I_{i-1,i}$ and $I_{i,i+1}$, and the "skip 1" interferogram is $I_{i-1,i+1}$.
2. We compute the residual phase error for each triplet of interferograms that connect acquisition dates $i-1$, i, $i+1$: $R_{i-1,i,i+1} = I_{i-1,i+1} - I_{i-1,i} - I_{i,i+1}$.
3. For the first circuit of interferograms, the correction is $R_{0,1,2}/3$, and the corrected interferograms are computed as $C_{i,i+1} = I_{i,i+1} - R_{0,1,2}/3$. For all subsequent circuits, one of the interferograms ($I_{i-1,i}$) has already been corrected at a previous step, and the residual is divided between the remaining two, $C_{i,i+1} = I_{i,i+1} - R_{i-1,i,i+1}/2$.
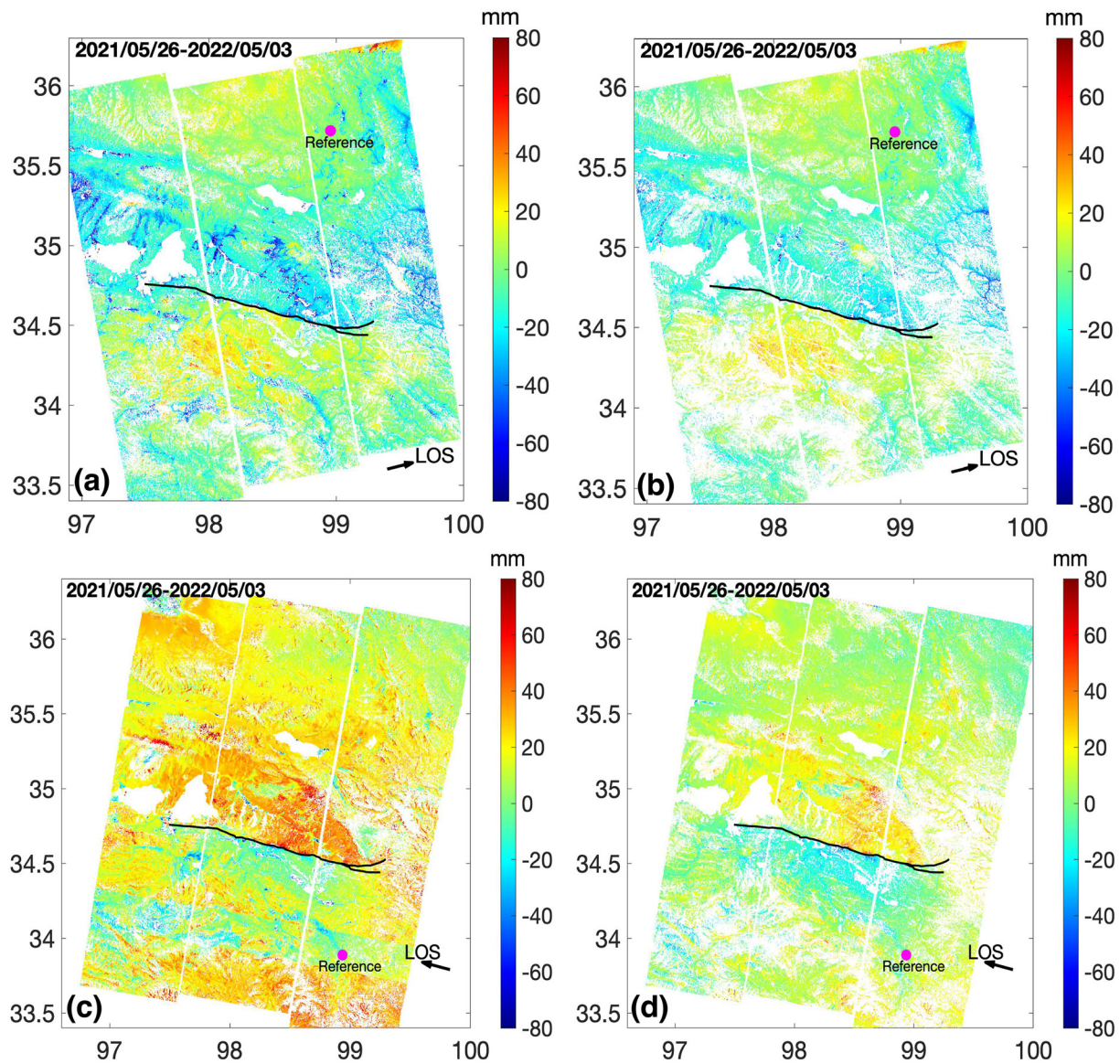
Figure 4. A comparison of (a, c) uncorrected and (b, d) corrected Sentinel-1 line of sight (LOS) displacements spanning ~1 year following the mainshock from (a, b) ascending track 99 and (c, d) descending track 106. Corrected displacements account for the systematic decorrelation noise. Positive LOS displacements correspond to surface motion away from the satellite. Observation periods are indicated in the top left corner of each panel. Magenta dots denote the reference points at which the LOS displacements are assumed to be zero. Black wavy line denotes the earthquake rupture. Arrows denote the LOS direction.

After correcting interferograms for the decorrelation noise, we use the common scene stacking method (Tymofyeyeva & Fialko, 2015) to estimate and remove the atmospheric and ionospheric artifacts. The time series of LOS displacements are then generated by a simple addition of the corrected sequential interferograms, without the need to solve a large system of equations. The "skip 1" interferograms are only used to estimate and correct for the decorrelation noise.

Figure 4 illustrates the cumulative LOS displacements calculated with and without corrections for the decorrelation noise. Atmospheric corrections using the common scene stacking method have been applied in both cases. As one can see, much of a signal apparent in Figures 4a and 4c is due to a systematic decorrelation noise. The corrected LOS displacements (Figures 4b and 4d) more clearly exhibit a postseismic deformation signal. We also note a reduction in phase discontinuity across the radar bursts (cf. Figures 4c and 4d at the latitude of ~34°N). The corrected LOS displacement anomalies have a spatial wavelength of ~50 km and are slightly asymmetric with respect to the fault trace (also see Figure 6a), with a larger amplitude on the north side of the fault.

This asymmetry may result from a northward fault dip (e.g., Fialko, 2004b; Fialko, Simons, & Agnew, 2001). An opposite polarity in the LOS displacements from the ascending and descending orbits (Figures 4b and 4d) indicates a predominantly left-lateral motion, expected of deep afterslip and viscoelastic relaxation below the brittle-ductile transition. The data also reveal discontinuous displacements across the fault trace in the central part of the earthquake rupture, indicative of shallow afterslip (Jin & Fialko, 2021). We further discuss contributions from different relaxation mechanisms in Section "Modeling of postseismic deformation."

Because of a limited number of ALOS-2 acquisitions in the post-seismic epoch (see Table S1 in Supporting Information S1), we only used ALOS-2 data to independently verify and validate results of our analysis of Sentinel-1 data. We generated 4 ALOS-2 interferograms originating the first post-event data take (4 June 2021). We estimated and removed ionospheric contributions using the split-spectrum method (Gomba et al., 2015). Figure S5 in Supporting Information S1 shows the original and corrected postseismic ALOS-2 interferogram having the longest time span (04 June 2021–14 January 2022). Figure S6 in Supporting Information S1 shows a comparison of LOS displacements from ALOS-2 and Sentinel-1 data across the central part of the earthquake rupture. The data are in general agreement, and both clearly show contributions of shallow afterslip as well as a longer-wavelength postseismic deformation (Figure S6b in Supporting Information S1).

3.2. GNSS Data

The GNSS data are from a network deployed and operated by the China Earthquake Administration. The data span 1 year after the earthquake. We computed daily positions with respect to stable Eurasia using GAMIT/GLOBK (Herring et al., 2016). The processed position time series reveal postseismic transients, as well as seasonal variations and offsets due to local earthquakes or site artifacts. To isolate the postseismic deformation signal, we post-processed the data as follows (e.g., Fialko & Jin, 2021):

1. We first removed obvious offsets by computing a difference between displacements averaged over 3-day intervals before and after the identified offsets.
2. We estimated the best-fit linear trends to the two-year (20 May 2019–21 May 2021) pre-earthquake time series, and subtracted it from the respective time series for each site and each displacement component (east, north, up).
3. We repeated step 1 to fix any remaining small-amplitude offsets.
4. We estimated and removed the seasonal deformation by performing a Principal Component Analysis (PCA) of the GNSS time series (Dong et al., 2006). Only the first principal component was subsequently used for each time series.

Figure 5 shows a comparison between the original and PCA-corrected GNSS time series. As one can see, the correction procedure efficiently removed offsets and seasonal signals. Uncertainties in the first principal component are reduced approximately by a factor of $\sqrt{2N}$, where N is the number of GNSS sites. Corrected time series reveal a gradually decelerating transient (Figure 5). Within the observation period, a strong earthquake (M6.6 7 January 2022 Menyuan earthquake) occurred within ∼35 km from site QHME (Yang et al., 2022). Postseismic displacements due to this event were rather small at site QHME, and negligible at the rest of the sites (Figure 5), so that we did not include the M6.6 event in our models of postseismic deformation. Figure S7 in Supporting Information S1 shows the corrected cumulative horizontal displacements 1 year after the mainshock. Similar to the InSAR data, the GNSS postseismic displacements exhibit a large-scale horizontal motion generally of the same sense as the coseismic displacements. Vertical components of the GNSS-derived displacements are dominated by seasonal variations, and have a large scatter even after the PCA corrections. Therefore they are not included in the subsequent analysis.

Figure 6 shows a comparison between the InSAR and GNSS time series at site QHMD that is closest to the earthquake rupture. Because the InSAR LOS displacements are intrinsically relative, we referenced all data to the GNSS site QHDL located at the periphery of the interferogram (Figure 6a). The InSAR timeseries are from the Sentinel-1 descending track 106. The GNSS data were projected on the satellite LOS using local incidence and heading angles. The InSAR and GNSS time series are in a good agreement, validating our algorithm for the InSAR timeseries. The early postseismic velocities are somewhat underestimated by the InSAR time series due to averaging inherent in the common scene stacking method (Tymofyeyeva & Fialko, 2015). The error is inversely proportional to the frequency of radar acquisitions. The agreement is worse for the ascending track that has less
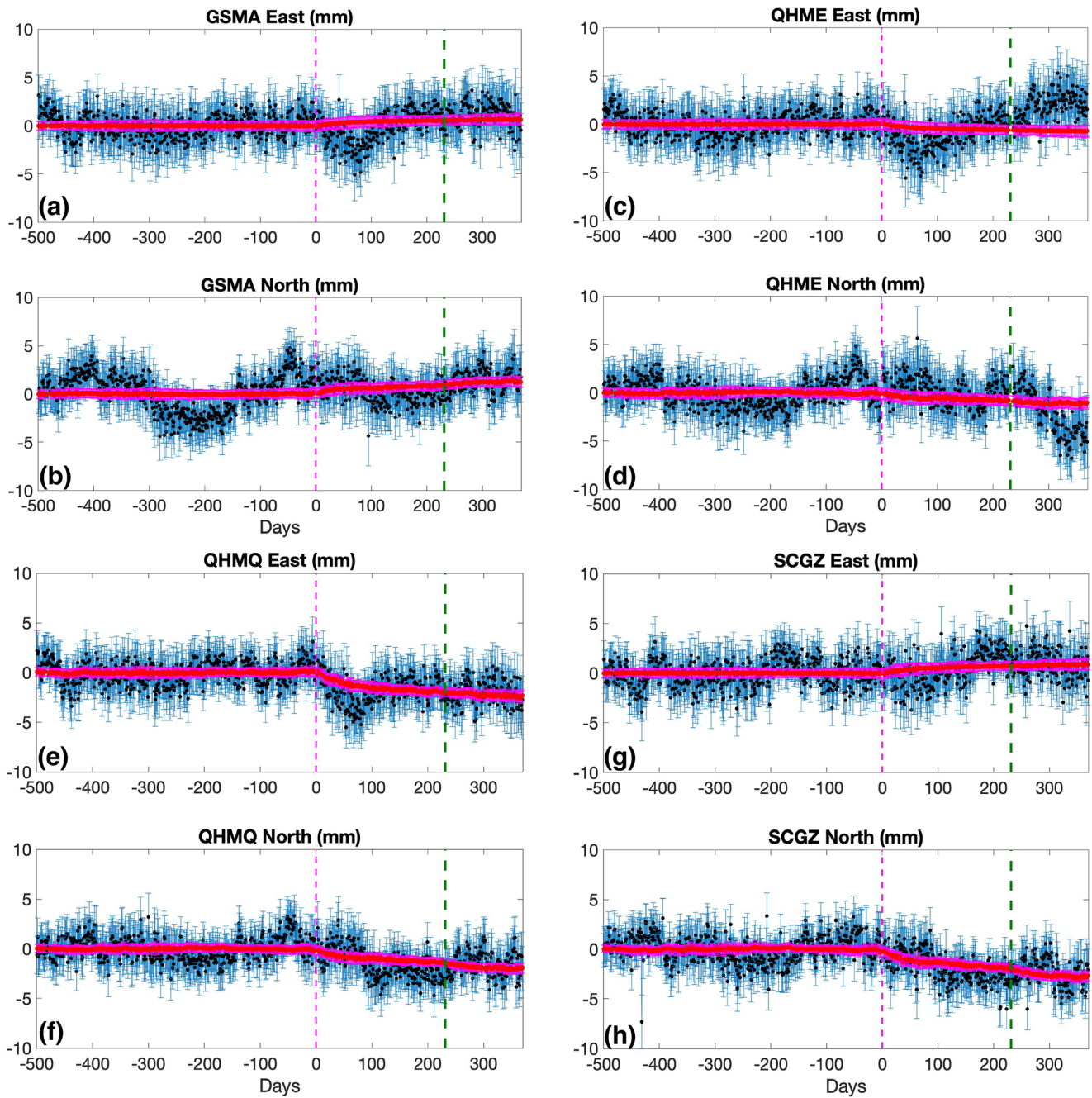
Figure 5. Global Navigation Satellite System (GNSS) time series for sites GSMA, GHME, QHMQ, and SCGZ. Black dots and blue error bars denote the daily GNSS solutions and their uncertainties, respectively. Magenta symbols denote the first principal component from the Principal Component Analysis analysis. The vertical magenta dashed line represents the time of the M7.4 Maduo earthquake, and the green dashed line represents the time of the 7 January 2022 M6.6 Menyuan earthquake.

frequent acquisitions compared to the descending track, highlighting the need for regular and frequent InSAR observations to monitor postseismic deformation.

4. Models of Postseismic Response

Hereafter, we refer to the data available at distances of <30, 30–200, and >200 km from the fault trace as the "near-field," "mid-field," and "far-field" data, respectively.
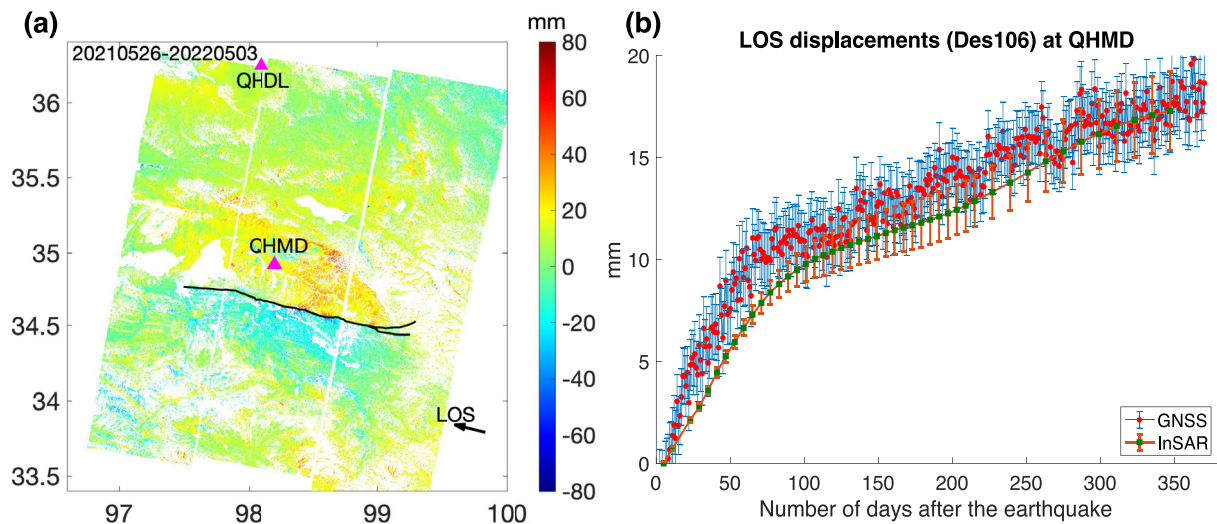
Figure 6. (a) Corrected cumulative Sentinel-1 line of sight (LOS) displacements spanning ~1 year following the mainshock from the descending track 106. Positive LOS displacements correspond to surface motion away from the satellite. Observation period is indicated in the top left corner. (b) A comparison of the Interferometric Synthetic Aperture Radar (InSAR) and Global Navigation Satellite System (GNSS) time series at the site QHMD. Green dots denote the InSAR data, and red dots denote the GNSS data projected on the satellite LOS. Error bars on the InSAR time series represent the standard deviation of LOS displacements for coherent pixels within 1 km from the site QHMD.

4.1. Poroelastic Rebound

Poroelastic re-equilibration of pore fluid pressure may cause surface displacements large enough to be detected by space geodetic observations (Fialko, 2004a; Jonsson et al., 2003; Peltzer et al., 1998). We evaluated potential contributions due to poroelastic rebound by differencing models of coseismic displacements under fully drained and undrained conditions. Our calculations used the coseismic slip model derived in Section "Kinematically consistent models of coseismic slip on non-planar faults" (Figure 3d). We assumed that the diffusion of pore fluids occurs at depths less than 15 km. The drained and undrained Poisson's ratios used in our calculations are 0.21 and 0.27, respectively. This range likely provides an upper bound on surface displacements that might result from poroelastic effects. Figure S8 in Supporting Information S1 shows the LOS displacements after a transition to a fully drained state is complete. Poroelastic models predict LOS displacements of several tens of millimeters, with dominant lobes of opposite polarity at the tips of the earthquake rupture (Figure S8 in Supporting Information S1). The InSAR data (Figures 4b and 4d), however, do not show such a displacement pattern above the estimated noise level (10–20 mm). The data also do not show small-scale regions of uplift or subsidence along the fault trace that might be indicative of poroelastic rebound in the fault step-overs (e.g., Jacobs et al., 2002; Peltzer et al., 1998). We therefore infer a negligible contribution from poroelastic rebound over 1 year after the earthquake.

4.2. Afterslip

As mentioned in section "InSAR data," the observed predominantly left-lateral displacements around the earthquake rupture (Figures 4 and 6a) reveal the occurrence of shallow, and possibly deep afterslip on the Maduo fault. We test this possibility using kinematic and dynamic models of afterslip.

4.2.1. Kinematic Inversions

We performed a series of kinematic inversions for a slip distribution on a fault that best explains the observed post-seismic displacements 1 year after the earthquake. Inversions use rectangular dislocations in a homogeneous elastic half-space (Okada, 1985) and a simplified piece-wise planar fault geometry described in Jin and Fialko (2021), extended in both strike and dip directions. The InSAR data are sampled using an adaptive quad-tree algorithm (K. Wang & Fialko, 2015). Figure S9 in Supporting Information S1 shows the best fitting afterslip distributions, and Figures S10 and S11 in Supporting Information S1 show a comparison between the data and model predictions. The kinematic afterslip model exhibits a reasonably good fit to the data within ~50 km from the rupture trace.

However, the model under-predicts displacements at far-field GNSS sites (Figure S11 and Table S2 in Supporting Information S1). A relatively small amount of shallow afterslip (~0.2 m) is found along the central fault segment, and most of the inferred afterslip occurs below the seismogenic rupture.

4.2.2. Stress-Driven Deep Afterslip

While kinematic inversions may provide a good fit to the data, the inferred slip distribution is not necessarily physical; for example, the stress drop due to afterlip may exceed the coseismic stress increase on a deeper aseismic root of the earthquake rupture. Based on a good performance of kinematic models (Figure S9 in Supporting Information S1), we further investigate a possible role of deep afterslip and evaluate in situ frictional properties of rocks in the respective aseismic part of the fault. Simulations were performed using Relax, a Fourier domain code based on a fictitious body force method (Barbot & Fialko, 2010a, 2010b).

We ignored the evolution effects and used a quasi-steady regularized form of the governing equation of rate and state friction under velocity-strengthening conditions (e.g., Barbot, Fialko, & Bock, 2009; Lapusta et al., 2000),

$$V = 2V_0 \sinh\left[\Delta\tau/(a-b)\sigma\right] \tag{1}$$

where $\Delta\tau$ is the driving Coulomb stress change, V_0 is the reference slip rate, a and b are the empirical constants, and σ is the effective normal stress acting on a fault. We assumed velocity-strengthening below the transition depth d_0 from the velocity weakening (VW) to velocity strengthening (VS) behavior of a fault interface.

Simulations were carried out for a wide range of d_0, V_0, and $(a-b)\sigma$. A model that best fits the near-field postseismic InSAR and GNSS time-series (Figure 10) suggests the following parameter values: $d_0 = 18$ km, $V_0 = 1.2$ m/yr, and $(a-b)\sigma = 1.1$ MPa. We further comment on the inferred value of V_0 in the "Discussion" Section. The same model also provides a qualitative fit to the GNSS time series from more distant sites (e.g., QHMQ and QHDL, see Figure S12 in Supporting Information S1). Figure 8 shows a comparison between the observed and modeled cumulative displacements at the far-field GNSS sites. The best-fit deep afterslip model is able to explain the observed amplitudes of surface displacements at most of the GNSS sites.

Assuming the effective normal stress on the fault $\sigma = 100$ MPa, the corresponding rate-and-state frictional parameters are $a - b = 1.1 \times 10^{-2}$, somewhat higher than the typical values of $a - b$ reported in laboratory experiments (e.g., Marone & Scholz, 1988; Mitchell et al., 2013, 2016). Figure S13 in Supporting Information S1 shows the resulting afterslip distribution on the entire fault plane. As one might expect, the highest amplitudes of afterslip are produced below the area of highest coseismic slip at the eastern end of the earthquake rupture. An overall agreement between the data and predictions of a stress-driven afterslip model (Figures 7 and 8), suggests that afterlip could be one of the dominant mechanisms of postseismic deformation during the first year following the earthquake.

4.2.3. Shallow Afterslip

Our stress-driven afterslip simulations do not include shallow afterslip because Relax would require exceedingly dense grids to resolve small near-surface elements (Barbot & Fialko, 2010b). To better quantify the distribution of shallow afterslip, we use the residual LOS displacements after subtracting the best-fit model of stress-driven deep afterslip (Figures 7e and 7f). To avoid potential trade-offs with long-wavelength residuals, we only use residual displacements within 20 km from the fault trace, and perform kinematic inversions using the fault model of Jin and Fialko (2021) truncated below the depth of 6 km. Figure S14 in Supporting Information S1 shows a comparison between the data and model predictions. The kinematic shallow afterslip model reveals that postseismic creep is mostly concentrated in the central section of the earthquake rupture, in agreement with observations of early (first month following the earthquake) shallow afterslip (Jin & Fialko, 2021). Figure 9 shows a superposition of the inferred shallow and deep afterslip due to the Maduo earthquake, and a comparison to the coseismic slip distribution. Along the central section of the earthquake rupture, the largest shallow afterslip occurs next to areas of large coseismic slip, as expected. The lack of shallow afterslip in other areas may be due to variations in frictional properties of rocks comprising the uppermost crust. Figure S15 in Supporting Information S1 shows a comparison between kinematic and stress-driven afterslip models. The two models agree to the first order, however, the stress-driven afterslip model suggests a larger slip close to the coseismic area, as expected because of a large coseismic increase in shear stress. A kinematic model is not able to capture high slip gradients near the bottom of the seismogenic zone due to the applied smoothness constraints.
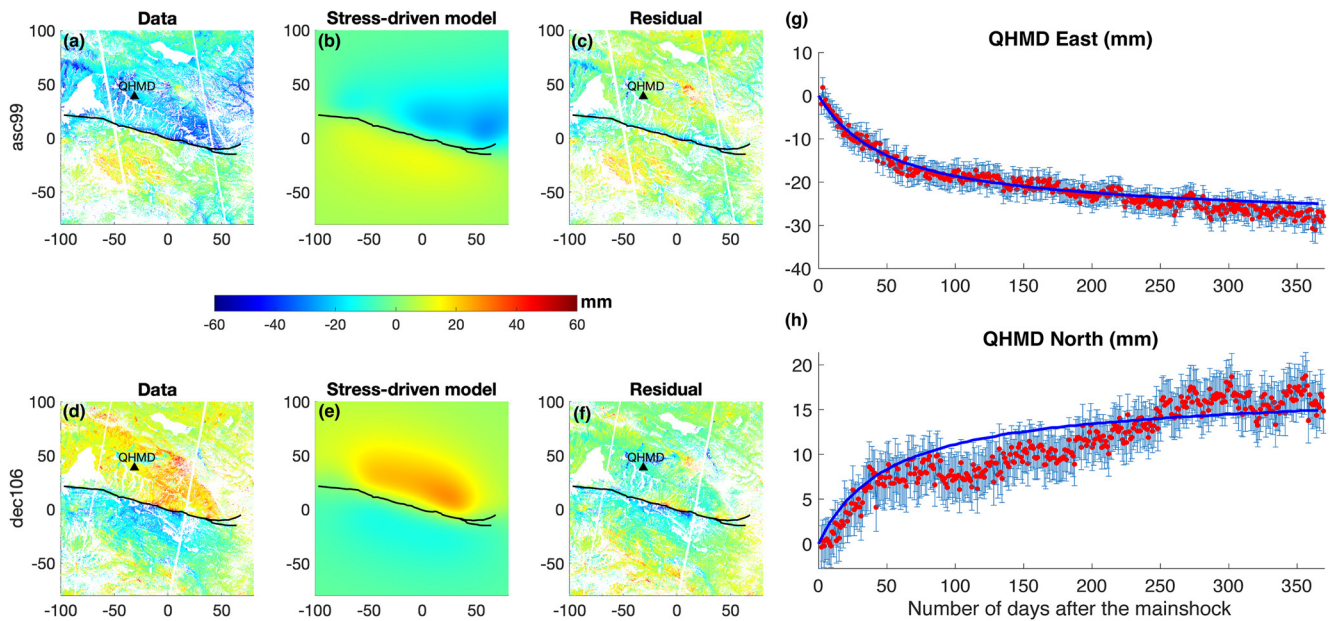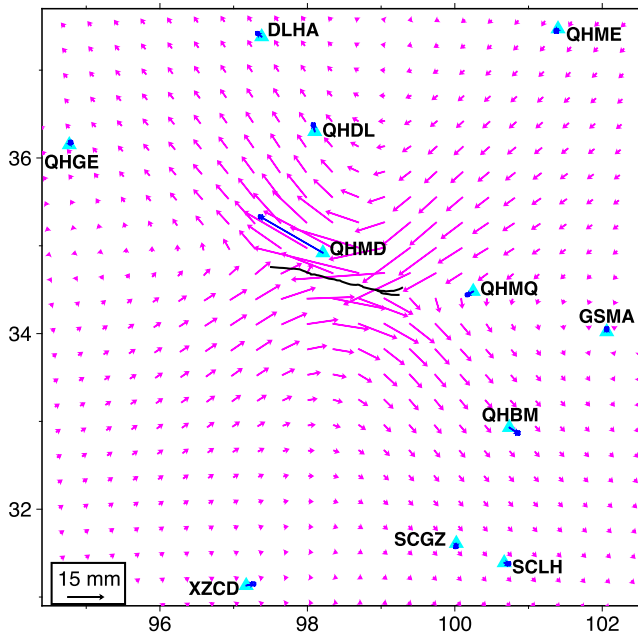
Figure 7. (a, d) Observed line of sight displacements, (b, e) prediction of the best-fit stress-driven afterslip model, (c, f) residuals after subtracting the model from the data. (a–c) Sentinel-1 ascending track 99. (d–f) Sentinel-1 descending track 106. (g, h) Observed and predicted time series of postseismic displacements at the Global Navigation Satellite System site QHMD.

4.3. Viscoelastic Relaxation

To investigate potential contributions of viscoelastic relaxation and constrain the effective viscosities of rocks below the brittle-ductile transition, we performed a suite of forward simulations assuming a vertically

Figure 8. Observed (blue arrows) and predicted (magenta arrows) postseismic displacements from the best-fit stress-driven afterslip model. Blue ellipses denote the observation uncertainties. Cyan triangles denote the Global Navigation Satellite System site locations.

stratified viscoelastic halfspace. Our viscoelastic models are parameterized in terms of the top elastic layer (that includes the upper crust) having thickness H, the lower crust having viscosity η_1, and the upper mantle having viscosity η_2. The assumed crustal thickness is 68 km, and the elastic layer thickness H is varied from 20 to 48 km (Xiong et al., 2010). Simulations were performed using Relax (Barbot & Fialko, 2010a) and PSGRN-PSCMP (R. Wang et al., 2006). To evaluate the fit of each viscoelastic model, we used the time series of GNSS displacements, as well as cumulative LOS displacements spanning 1 year after the earthquake (Figures 4b and 4d).

4.3.1. Maxwell Rheology

We first tested a model assuming a linear Maxwell rheology for both the lower crust and upper mantle. We performed a grid search over the model parameters H, η_1, and η_2. Figure S16 in Supporting Information S1 shows the predicted horizontal displacements at site QHMD. The best performing model ($H = 30$ km, $\eta_1 = 10^{18}$, and $\eta_2 = 10^{20}$ Pa s) is able to match the observed orientation and amplitude of surface displacements over a period of 1 year following the earthquake. However, none of the models are able to fit the time evolution of surface displacements: models that can fit the amplitude of displacements 1 year after the event strongly under-predict the initial velocity, and models that are able to fit the initial velocity strongly over-predict total displacements 1 year after the event (Figure S16 in Supporting Information S1). Thus models assuming a linear Maxwell rheology thus fail to explain the observed deformation transient, similar to findings from other major earthquakes (e.g., Freed & Bürgmann, 2004).
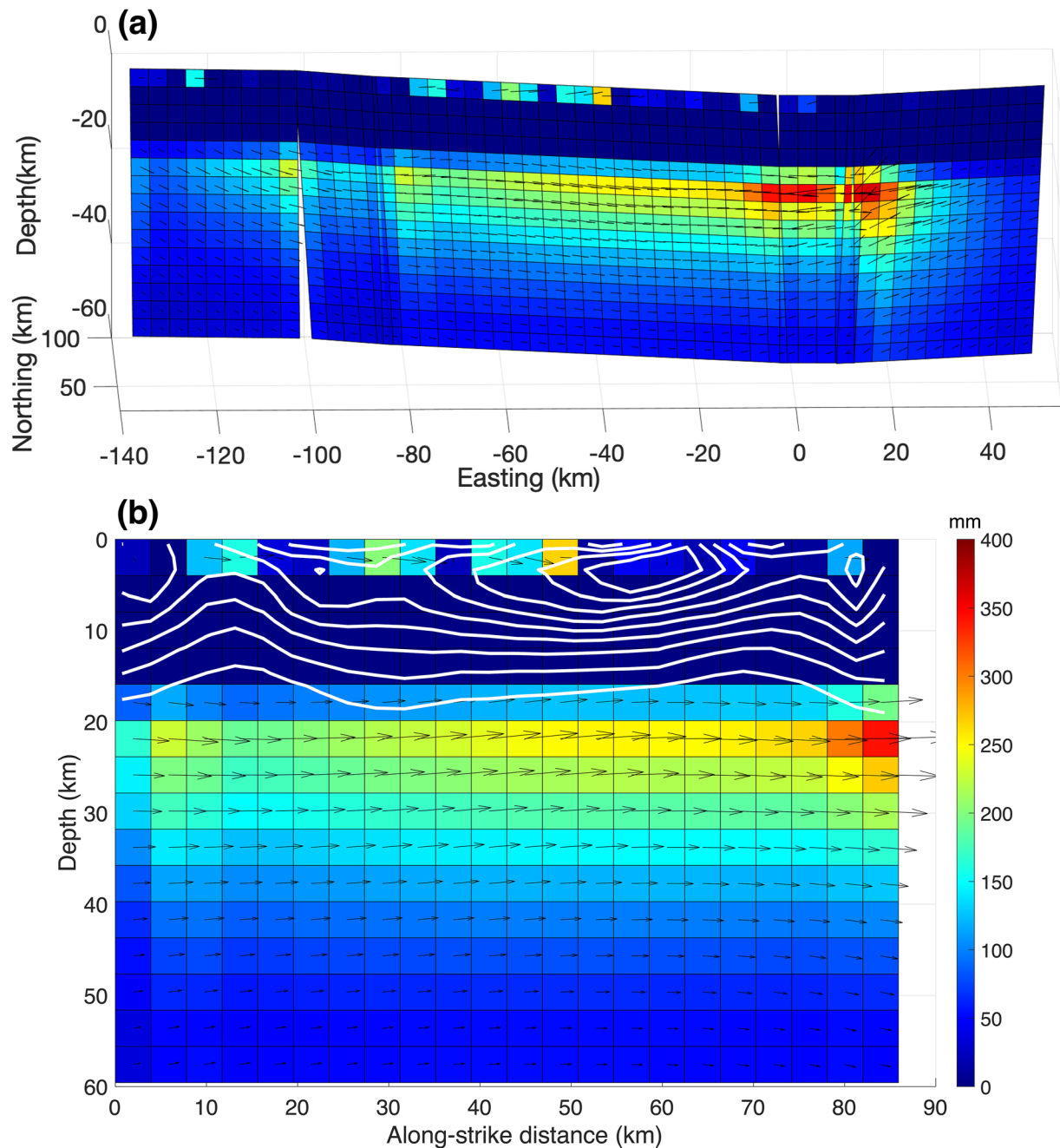
Figure 9. (a) A superposition of the best-fit kinematic model of shallow afterslip and stress-driven model of deep afterslip. (b) Afterslip distribution on the central segment. Colors denote the amplitude of slip in millimeters. Arrows denote slip direction for each slip patch. White contours denote the coseismic slip at 0.5 m intervals, starting at 0.5 m.

4.3.2. Burgers Rheology

A possible variation of a linear viscoelastic rheology is the Burgers (bi-viscous) rheology (e.g., Pollitz, 2003). The latter can be represented by a combination of the Maxwell viscoelastic material with "steady-state" viscosity η_M and shear modulus μ_M, and the Kelvin-Voight material with "transient" viscosity η_K and shear modulus μ_K. Each viscoelastic material is characterized by its own relaxation time, which may potentially account for the initial rapid transient, followed by a slow one. During the initial transient period, the effective shear modulus of the Burgers material relaxes from the instantaneous Maxwell value μ_M to a long-term value $\mu_M\mu_K/(\mu_M + \mu_K)$. The relaxation of the shear modulus is defined as the ratio α of the long-term to the initial shear modulus, $\alpha = \mu_K/(\mu_M + \mu_K)$.
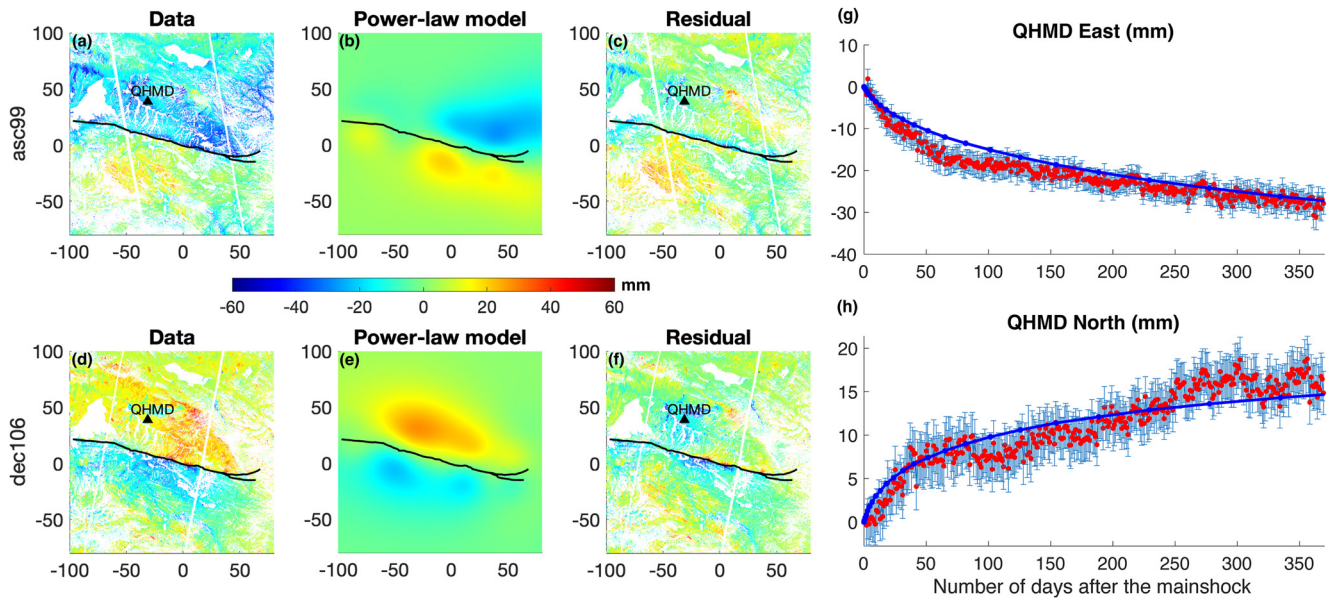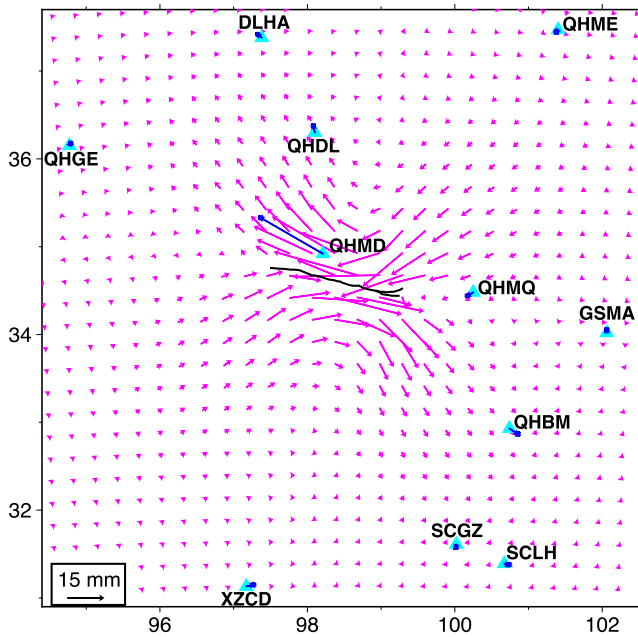
Figure 10. Same as Figure 7, for the best-fit viscoelastic relaxation model assuming a power-law rheology.

We used the same 3-layer (i.e., including the elastic layer, and viscoelastic lower crust and upper mantle) model as described above to perform a grid search over the model parameters. Figure S17 in Supporting Information S1 shows the predicted horizontal displacements at the GNSS site QHMD for a range of α and η_K. The steady-state viscosity η_M is fixed at 10^{19} Pa s in all simulations. As one can see from Figure S17a in Supporting Information S1, assuming $\alpha = 0.5$ (i.e., $\mu_M = \mu_K$) results in a poor fit to the data regardless of the assumed value of η_K. Previous studies of postseismic deformation in northern Tibetan Plateau assumed the value of α of 2/3 (Ryder et al., 2011). Our results (Figures S17b and S18 in Supporting Information S1) suggest that the bi-viscous lower crust with $\alpha = 0.75$, $\eta_K = 10^{18}$, and $\eta_M = 10^{19}$ Pa s could explain both the near-field InSAR displacements and time series at the GNSS site QHMD reasonably well. However, the respective model under-predicts displacements at distant (>150 km) GNSS sites (Figure S19 in Supporting Information S1), as estimated from our PCA (Figure 5 and Figure S7 in Supporting Information S1).

4.3.3. Power-Law Rheology

Another candidate mechanism is a power law flow, for which the deviatoric strain rate is proportional to τ^n, where τ is the deviatoric stress, and n is the power exponent (for typical rock types, n varies between 2 and 5). Compared to a linear ($n = 1$) rheology, the effective viscosity of a power-law material is not a material property, and increases with a decreasing deviatoric stress. This can potentially explain the observed rapid deformation followed by a slowly decaying transient (Figures 5 and 6b). We conducted several tests to evaluate the sensitivity of surface displacements to the assumed values of n for the lower crust and upper mantle. We found that changes in n for the upper mantle have a negligible effect on the predicted histories of surface displacements. Consequently, we assumed $n = 1$ and a steady-state viscosity $\eta_2 = 10^{20}$ Pa s for the upper mantle. Hereafter, the effective stress-dependent viscosities of the lower crust η_1^τ are reported for $\tau = 2$ MPa (the reference stress taken to be of the order of the coseismic stress change; the absolute deviatoric stress is not known, but the effective power-law viscosity can be calculated given η_1^τ and n for any other value of τ).

Figure 10 and Figure S20 in Supporting Information S1 show predicted horizontal displacements at the GNSS site QHMD for a range of model parameters H, n and η_1^τ. Because of a decay of coseismic stress changes with depth, and the associated increase in the effective viscosity, models that assume a relatively thick elastic layer ($H \sim 25$ km or greater) under-predict the magnitude of surface displacements (Figure S20a in Supporting Information S1); the preferred values of H are 20–21 km. The models also favor a relatively high value of stress exponent ($n = 4$–4.5) in order to fit the entire time series of displacements (Figure S20b in Supporting Information S1). Figure 10 and Figure S21 in Supporting Information S1 show predictions of the best-fit power-law model, which can reasonably well explain both InSAR data and GNSS data from other "mid-field" sites such as

Figure 11. Same as Figure 8, for the best-fit viscoelastic relaxation model assuming a power-law rheology.

QHMQ and QHDL (see Figure 1). For the best-fitting parameters $H = 21$ km and $n = 4$, and the reference deviatoric stress $\tau = 2$ MPa, the effective viscosity of the lower crust is $\eta_1^\tau = 3.2 \times 10^{15}$ Pa s. Power-law models fit far-field GNSS cumulative displacements a little bit better than the one assuming biviscous rheology (Figure S22 and Table S2 in Supporting Information S1), but they still under-predict the amplitude compared to the deep afterslip model (Figure 11, Table S2 in Supporting Information S1).

5. Fully Coupled Afterslip and Viscoelastic Relaxation Models

Given that several candidate mechanisms are able to explain general features of postseismic deformation (Figures 7 and 10, Figure S18 in Supporting Information S1), it is likely that more than one mechanism was involved in generating the observed transient. To explore trade-offs between model parameters, we used a coupled model incorporating stress-driven afterslip and viscoelastic relaxation governed by a power-law rheology. Simulations were performed using Relax. Because of a high-dimensional parameter space, our initial choice of parameters was guided by best-fit models of single relaxation mechanisms: depth of a transition from VW to VS friction $d_0 = 18$ km, thickness of elastic layer $H = 21$ km, power-law exponent $n = 4$. The varied parameters were the afterslip reference rate V_0, the rate-and-state frictional parameter $(a - b)\sigma$, and the effective viscosity of the lower crust η_1^τ. In each simulation, we computed χ^2 misfits to the GNSS time series for sites located in the mid-field. As expected, there is a tradeoff between contributions of afterslip and the bulk viscoelastic relaxation (in particular, parameters V_0 and η_1^τ, see Figure 12a). A stronger lower crust with robust afterslip (high η_1^τ and V_0, outlined by a blue dashed line in Figure 12a), or a weaker lower crust with a smaller contribution of afterslip (low η_1^τ and V_0, outlined by a black dashed line) yield similar fits to the GNSS time series. We find that the rate parameter $(a - b)\sigma$ does not exhibit a strong trade off with the effective viscosity of the lower crust (Figure 12b).
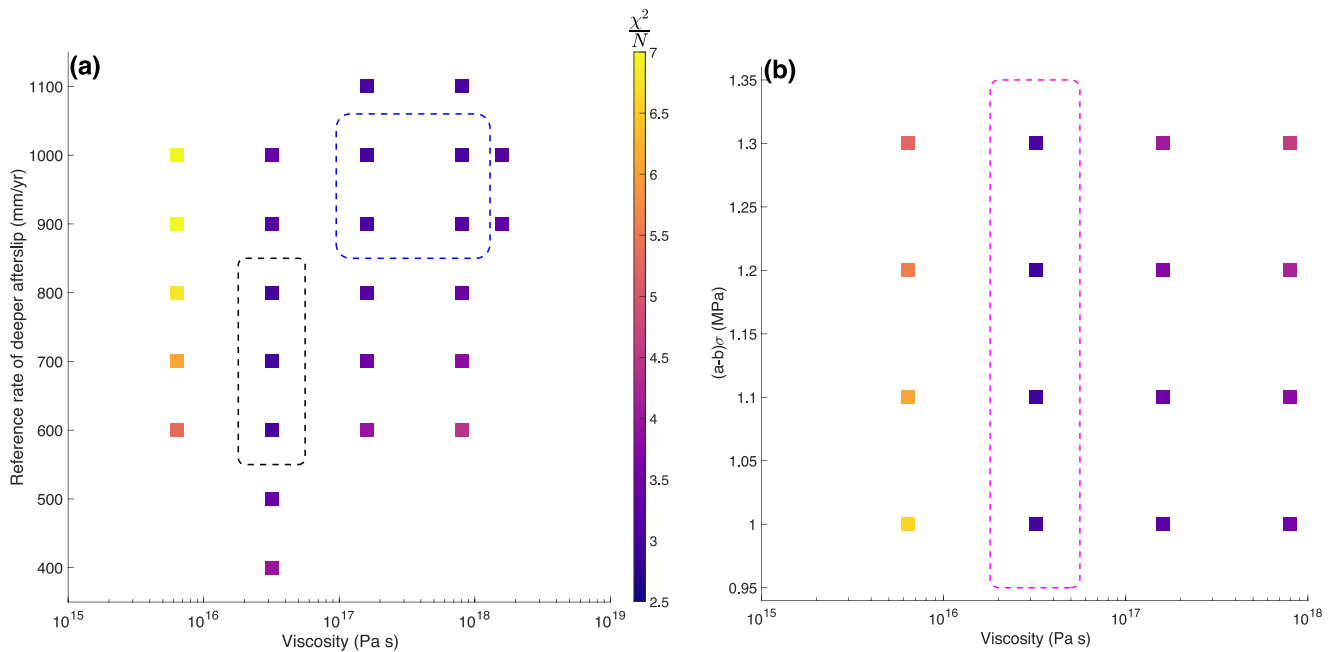
Figure 12. The reduced χ^2 misfits (χ^2/N) to Global Navigation Satellite System (GNSS) time series for a range of coupled models with variable reference slip rate V_0, $(a - b)\sigma$, and effective viscosity of the lower crust η_1. Color dashed contours denote the range of model parameters that yields the best-fit to GNSS time series. (a) The value of $(a - b)\sigma$ is fixed at 1.1 MPa. (b) The value of V_0 is fixed at 700 mm/yr.

Results of our calculations using coupled models (Figure 12) suggest the best-fit parameters $V_0 = 700$ mm/yr, $(a - b)\sigma = 1.1$ MPa and $\eta_1^\tau = 3.2 \times 10^{16}$ Pa s, which yield the misfit of $\chi^2/N = 2.9$. Our best-fit afterslip ($V_0 = 1{,}200$ mm/yr, $(a - b)\sigma = 1.1$ MPa) and power-law ($\eta_1^\tau = 3.2 \times 10^{15}$ Pa s) models yield similar misfits (3.2 and 3.0, respectively). Similar to the individual afterslip and power-law visco-elastic models, the coupled model shows a good agreement with the near-field InSAR and GNSS data (Figures S23–S25 in Supporting Information S1). It also exhibits a better fit to the far-field GNSS data compared to purely visco-elastic power-law models (Figure S26 and Table S2 in Supporting Information S1).

For completeness, we also considered a coupled model including afterslip and a linear Maxwell viscoelasticity. A possible justification for such a model would be that the near-field deformation is dominated by afterslip, but the far-field deformation is primarily due to viscoelastic relaxation. Because a linear Maxwell rheology is more efficient at generating far-field motion compared to the power-law rheology, the former might be able to explain the inferred amplitudes of far-field displacements (Figure S7 in Supporting Information S1), given that the details of temporal evolution are hard to resolve due to a small signal to noise ratio (Figure 5). Holding the other parameters fixed to the preferred values found in the single-mechanism model exploration, we performed a grid search over three model parameters: afterslip reference rate V_0, Maxwell viscosity of the lower crust η_1, elastic thickness H, and computed χ^2 misfits using the GNSS time series, as before (Figure S27 in Supporting Information S1). A misfit increases when the viscosity η_1 decreases from 10^{19} to 10^{18} Pa s (see Figure S27a in Supporting Information S1) due to an over-prediction of displacements in the near field. The best-fit coupled model ($V_0 = 700$ mm/yr, $\eta_1 = 10^{19}$ Pa s, $H = 30$ km) is able to fit the amplitude of displacements in the near- and mid-field 1 year after the earthquake (Figure S26b and Table S2 in Supporting Information S1). However, such a model fails to explain the well-resolved details of temporal evolution, in particular high velocities at the early stages of postseismic relaxation (Figure S27a and Table S2 in Supporting Information S1); it also under-predicts the amplitude of the east component of displacements at the site QHMQ which has a high signal to noise ratio (Figure S28b in Supporting Information S1). Because the characteristic relaxation time for the inferred viscosity of 10^{19} Pa s is much greater than the time span of observations, these estimates essentially provide a lower bound on the effective viscosity of the lower crust, which may be higher still (K. Wang & Fialko, 2014, 2018; Jin et al., 2022). These results suggest that the deep afterslip (or, more broadly, localized shear beneath the earthquake rupture) is required by the data, even in the presence of viscoelastic relaxation in the bulk of the lower crust. We did not consider a coupled model that combines the Burger's rheology and afterslip, as the Burger's model produces a worse fit to the GNSS data compared to the afterslip model, and smaller far-field displacements compared to the Maxwell model (Figure S22 and Table S2 in Supporting Information S1).

6. Discussion

Our analysis of postseismic deformation excited by the 2021 M7.4 Maduo earthquake reveals a robust and far-reaching transient dominated by a left-lateral shear (Figures 4b, 4d, and 8). The near- and mid-field (within one rupture length, i.e., <200 km) postseismic displacements do not show a clear contribution of poroelastic rebound, but could be explained by afterslip, viscoelastic flow in the lower crust, or some combination of the latter two mechanisms. The poroelastic rebound thus appears to accompany some but not all large shallow earthquakes (Barbot, Hamiel, & Fialko, 2008; Fialko, 2004a; Gonzalez-Ortega et al., 2014; Jonsson et al., 2003; Peltzer et al., 1998; K. Wang & Fialko, 2018), possibly due to variations in porosity and/or fluid saturation of a pore space. The time series of surface displacements rule out a linear Maxwell rheology as the dominant mechanism. Either bi-viscous or power-law rheologies are able to explain the near-field data reasonably well (Figure S18 in Supporting Information S1 and Figure 10). Distinguishing between the two candidate rheologies based on details of time-dependent response is challenging even if multi-year timeseries of postseismic deformation are available (e.g., Takeuchi & Fialko, 2013). In case of a bi-viscous rheology, our models suggest transient and steady-state viscosities of the order of 10^{18} and 10^{19} Pa s, respectively. This is similar to previously reported constraints on the effective viscosity of the lower crust from postseismic (e.g., D. Zhao et al., 2021a), lake loading (e.g., Henriquet et al., 2019), and magma loading (e.g., Pearse & Fialko, 2010) modeling studies. However, we find that viscoelastic models that fit the near-field data tend to under-predict the far-field displacements determined from the PCA of the GNSS data (Table S2 in Supporting Information S1). For example, in case of models that assume a power-law rheology, a large stress exponent needed to explain strong variations in surface velocity (Figures 10g and 10h) gives rise to large variations in the effective viscosity as a function of distance from the earthquake rupture, and a reduced ratio of far-field to near-field displacements (e.g., Barbot & Fialko, 2010b). In
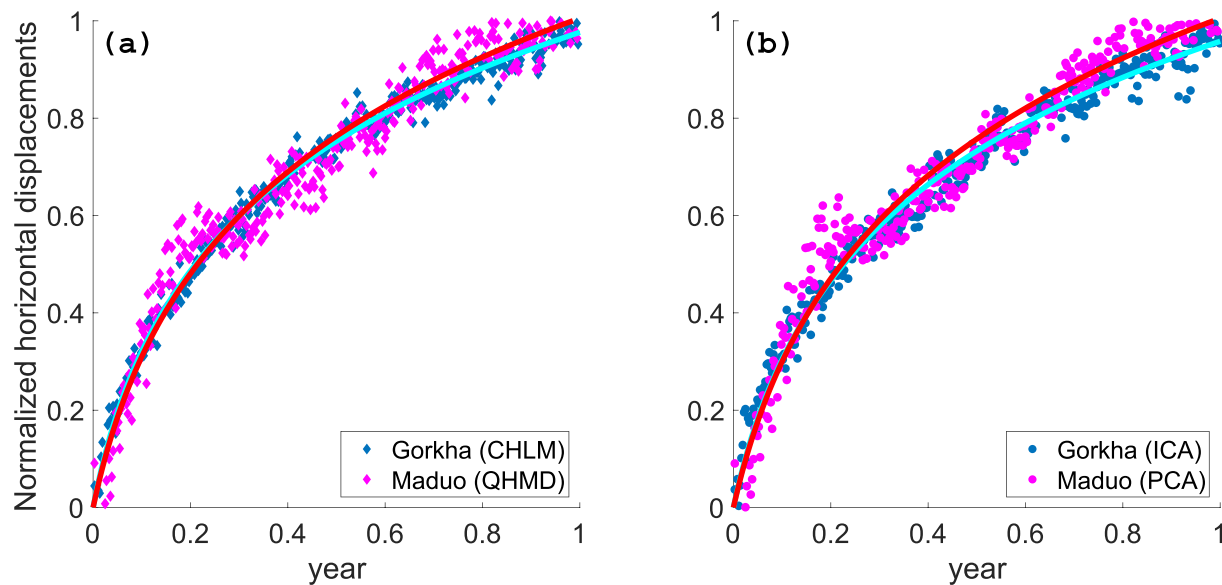
Figure 13. A comparison of time dependence of postseismic transients due to the Maduo (teal dots) and the 2015 Gorkha, Nepal (magenta dots) earthquakes. (a) Displacement time series from the closest Global Navigation Satellite System (GNSS) site (CHLM in the case of the Gorkha earthquake and QHMD in the case of the Maduo earthquake). (b) The first principal component of the Independent Component Analysis (Gorkha earthquake) and Principal Component Analysis (Maduo earthquake) of a local network of GNSS sites. Time series have been normalized by the amplitude of displacements 1 year after the respective events. Red and blue lines denote the best-fitting impulse response functions (see Equation 2) for the Maduo and Gorkha earthquakes, respectively.

addition, a large stress exponent ($n > 4$) implies that rocks in the lower crust deform via dislocation creep, which in turn requires high temperatures and high deviatoric stresses on the order of tens of megapascals or more (e.g., Bürgmann & Dresen, 2008; Wilks & Carter, 1990). Theoretical arguments and various observational constraints suggest similar values of average deviatoric stresses supported by the upper and lower crust in regions of active faulting (e.g., Fialko, 2021; Fialko, Rivera, & Kanamori, 2005; Takeuchi & Fialko, 2012). However, laboratory data suggest a flow law of a wet feldspar-dominated lower crust with a stress exponent $n \leq 3$ (e.g., Bürgmann & Dresen, 2008), smaller than that inferred from our best-fit power-law models (Figure 10). Thus it remains unclear if a power-law rheology is a viable mechanism for viscous creep in the lower crust. A significant contribution of stress-driven afterslip extending through much of the lower crust appears to be necessary to explain the data (Figures 7 and 8, Figure S26 and Table S2 in Supporting Information S1). Our estimate of the elastic thickness beneath the NE Tibetan margin of 20–25 km (Figures S20a and S27a in Supporting Information S1) is consistent with the depth extent of seismicity (Figure 2) and recent studies (e.g., Guo et al., 2022).

Further insights can be gained from a detailed consideration of the functional form of the displacement time series. Figure 13 shows a comparison of the temporal evolution of horizontal postseismic displacements due to the 2021 Maduo earthquake and the 2015 M7.6 Gorkha (Nepal) earthquake that occurred at the southern boundary of the Tibetan Plateau (K. Wang & Fialko, 2015, 2018). The displacements are normalized by their mean value 1 year after the mainshock. The time series show a remarkable similarity, suggesting a common mechanism. In case of the Gorkha earthquake, K. Wang and Fialko (2018) demonstrated that the near-field postseismic deformation resulted from afterslip below the seismogenic zone. A nearly identical time dependence (Figure 13) suggests that afterslip also dominated the near-field response in case of the Maduo earthquake. Furthermore, the observed time evolution of postseismic displacements for both events is well approximated by an impulse response function of the VS friction (Barbot, Fialko, & Bock, 2009),

$$s(t) = A\left[1 - \frac{2}{k}\coth^{-1}\left(e^{t/t_0}\coth\frac{k}{2}\right)\right], \tag{2}$$

where t is time, A is the strain drop (stress drop $\Delta\tau$ normalized by the shear modulus μ), $k = \Delta\tau/(a-b)\sigma$ is a parameter that controls the degree of nonlinearity during slip evolution, and t_0 is the characteristic relaxation time. Parameters A, k, and t_0, were estimated by fitting the normalized time series (Figure 13) using Equation 2 and a nonlinear least-squares solver. The best-fit values are $A = 2.50$, $k = 6.24$, and $t_0 = 23.52$ years in case of

the Maduo earthquake, and $A = 2.32$, $k = 6.44$ and $t_0 = 23.58$ years in case of the Gorkha earthquake. Both time series can be equally well fitted assuming an impulse response function for the power-law creep (Barbot, Fialko, & Bock, 2009),

$$ s(t) = A \left[1 - \left(1 + \frac{t}{t_0} \right)^{-1/(n-1)} \right]. \tag{3} $$

Because the observed deformation transient is still evolving 1 year after the event (Figure 13), best fitting models using Equation 3 exhibit a strong trade of between the stress exponent n and the characteristic relaxation time t_0. For example, for $n = 4$, the inferred relaxation time is $t_0 = 0.15$ years, but essentially the same fit can be obtained for example, for $n = 40$, and $t_0 = 0.07$ years. Continued observations will place tighter constraints on the model parameters. A comparison shown in Figure 13 lends support to the hypothesis that the robust postseismic transient due to the Maduo earthquake was dominated by deep afterslip, and furthermore suggests that frictional properties of faults below the seismogenic zone are similar for faults that hosted the 2015 Gorkha and the 2021 Maduo earthquakes.

Our best-fit stress-driven models (Figure 12) suggest a relatively high value of the reference slip rate $V_0 = 1.2$ m/yr, which is significantly larger than some previous estimates from studies of postseismic deformation (Barbot, Fialko, & Bock, 2009; Perfettini & Avouac, 2007), but in agreement with other studies including the aftermath of the 2017 M7.3 Sarpol-e Zahab earthquake (K. Wang & Bürgmann, 2020, $V_0 = 1.42$ m/yr for the updip section of the fault) and the 2001 M7.8 Kokoxilli earthquake (D. Zhao et al., 2021a, $V_0 = 3.2$ m/yr). There are different views about the physical meaning of V_0. It was interpreted as representing the pre-earthquake (i.e., interseismic) slip rate (Perfettini & Avouac, 2007), the initial afterslip rate immediately after the earthquake, or rock properties that control the evolution of afterslip, irrespective of the interseismic slip rate (Barbot, Fialko, & Bock, 2009). The interseismic slip rate in case of the Maduo fault is less than 2 mm/yr (Fang et al., 2022; Guo et al., 2022; Y. Zhu et al., 2021), far smaller than our estimated value of V_0. We therefore conclude that V_0 does not represent the interseismic slip rate.

There's been some debate regarding relative contributions of afterslip and viscoelastic relaxation due to large earthquakes in and around Tibetan Plateau (Huang et al., 2014; Jin et al., 2022; Ryder et al., 2011; K. Wang & Fialko, 2014, 2018; D. Zhao et al., 2021a). Separating the respective contributions is particularly challenging in case of long strike-slip ruptures (e.g., Barker, 1976; Savage, 1990), given a limited knowledge of in situ frictional and rheologic properties of rocks below the brittle-ductile transition. Previous studies that considered both afterslip and viscoelastic relaxation (e.g., Huang et al., 2014; D. Zhao et al., 2021a) in general found that inclusion of afterslip increases the inferred effective viscosity of ductile strata, compared to purely viscoelastic models. These studies, however, did not allow for a full coupling between the two mechanisms.

Our study systematically explored a wide range of possible relaxation mechanisms, both individually and in combination, accounting for the relevant mechanical interactions. Based on a number of simulations, we conclude that the observed postseismic transient over 1 year following the Maduo earthquake was dominated by afterslip. In order to explain the mid-to-far-field deformation (Figure 8), stress-driven afterslip needs to extend throughout much of the lower crust (Figure 9). It is perhaps unreasonable to expect that a fault may maintain a slip interface at such considerable depths. Mature faults however may transition to localized shear zones that kinematically would be indistinguishable from a slip interface (e.g., Takeuchi & Fialko, 2012, 2013). Our inference of a "deep afterslip" therefore should be understood broadly as "a stress-driven localized shear beneath the seismogenic rupture".

It is also of interest to quantify the contribution of shallow afterslip (Figure 9) in the context of a shallow slip deficit (SSD) problem (Fialko, Sandwell, et al., 2005; Jin & Fialko, 2021). Coseismic slip models of the Maduo earthquake indicate that surface slip is about 30% smaller than slip at depth of 3–5 km, similar to inferences from many other major strike-slip earthquakes world-wide (Figure 14a). Jin and Fialko (2021) documented shallow afterslip that occurred in the first month following the mainshock, suggesting a possibility that most of the coseismic deficit could be taken up via aseismic creep in the velocity-strengthening uppermost crust. We use results of kinematic inversions for a shallow slip distribution during the first year after the Maduo earthquake (Figure 9) to determine what fraction of the coseismic deficit was compensated by shallow creep. Figure 14b shows a comparison of the coseismic slip averaged along strike, as a function of depth (blue line), and the shallow afterslip that occurred over 1 year (yellow area). We estimate that the shallow afterslip accounts for less than 5%
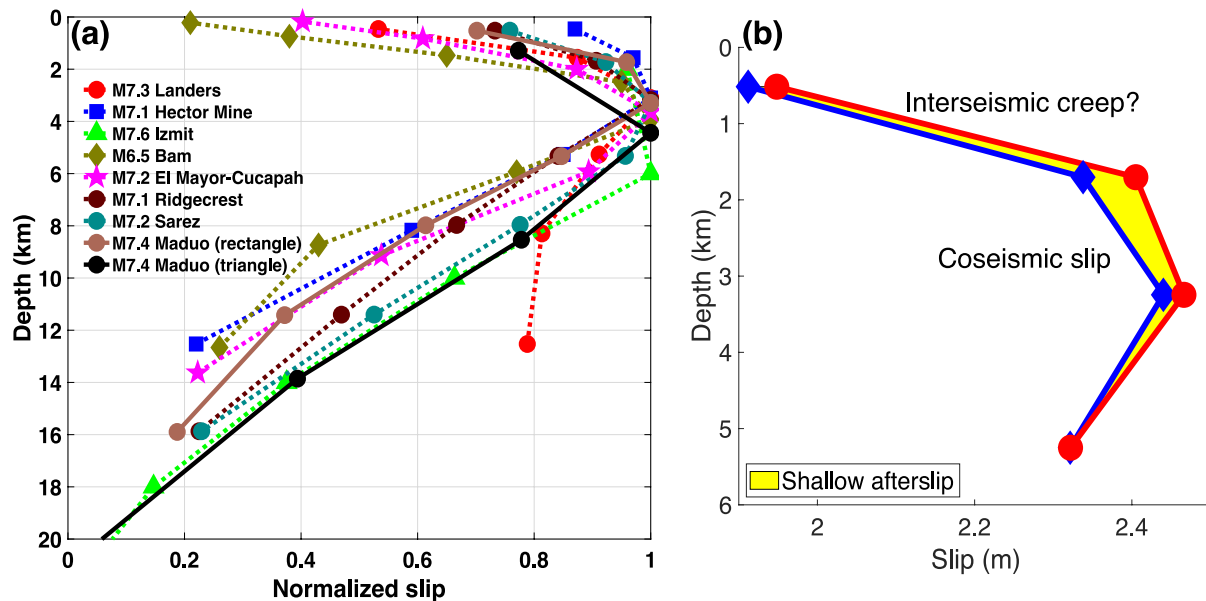
Figure 14. (a) Along-strike averaged normalized coseismic slip as a function of depth for the 2021 M7.4 Maduo earthquake: brown circles and solid lines correspond to rectangular discretization, and black circles and solid lines correspond to triangular discretization (see Figure 3). Color symbols and dashed lines correspond to slip distributions from other strike-slip earthquakes: Landers (from Fialko (2004a)), Hector Mine (from Simons et al. (2002)), Izmit (from Hamiel and Fialko (2007)), Bam (from Fialko, Sandwell, et al. (2005)), El Mayor-Cucapah (from Gonzalez-Ortega et al. (2014)), Ridgecrest (modified from Jin and Fialko (2020), see Supporting Information S1), Sarez (from Jin et al. (2022)). (b) Coseismic slip due to the Maduo earthquake in the top 3 km (blue line), and shallow afterslip inferred from kinematic inversions of postseismic displacements (yellow area). Red curve represent the sum of coseismic slip and 1 year of shallow afterslip. The remaining deficit may be accommodated by some combination of interseismic creep and off-fault yielding due to dynamic stress changes.

of the coseismic deficit. Although some shallow afterslip may still occur beyond the first year of deformation, the log-exponential nature of the signal (Equation 2) indicates that the latter is dominated by the early deformation period. Some of the remaining deficit may be taken up by interseismic creep. Given a low long-term slip rate on the Maduo fault, the associated shallow creep rate may be a fraction of a millimeter per year, likely below the detection limit (Fang et al., 2022; Pan et al., 2022; D. Zhao et al., 2021b). This average rate includes contributions from both quasi-steady creep, and episodic slow slip events (e.g., Li et al., 2023; Tymofyeyeva et al., 2019; M. Wei et al., 2013), if any. The remaining apparent deficit may be attributed to unaccounted effects of a low-rigidity fault damage zone (e.g., Barbot, Fialko, & Sandwell, 2008) or off-fault yielding due to dynamic stress perturbations (Antoine et al., 2021; Kaneko & Fialko, 2011; Roten et al., 2017).

7. Conclusions

The 2021 M7.4 Maduo earthquake occurred in the Bayan Har tectonic block in the northeast Tibetan Plateau. We presented space geodetic (InSAR and GNSS) observations and models of coseismic and postseismic deformation due to the earthquake. We derived a refined coseismic slip model using a non-planar fault geometry constrained by surface offsets and precisely relocated aftershocks. Time series of postseismic displacements spanning ~1 year after the mainshock reveal a broad (~50 km) region of left-lateral shear consonant with coseismic displacements. Postseismic displacements are discontinuous across the fault trace, indicating shallow afterslip. The largest postseismic LOS displacements of ~100 mm are observed at the east end of the earthquake rupture where the latter bifurcates into two sub-parallel strands. The shallow afterslip compensates for only a small fraction (<5%) of coseismic SSD. The remaining deficit could be attributed to interseismic creep, a compliant fault zone, or off-fault yielding due to dynamic stress perturbations. The longer-wavelength postseismic deformation is consistent with afterslip on a deep extension of the seismogenic fault, viscoelastic relaxation in the lower crust, or some combination of the two mechanisms. The observed spatio-temporal pattern of surface displacements suggests deep localized shear extending through much of the lower crust as the dominant mechanism.

Conflict of Interest

The authors declare no conflicts of interest relevant to this study.

Data Availability Statement

The post-processed data presented in this study are available at https://zenodo.org/record/7689859#.Y__JYOz-MKCc (Jin et al., 2023). Raw Sentinel-1 data are available from Alaska Satellite Facility (https://asf.alaska.edu/data-sets/sar-data-sets/sentinel-1/) (ASF, 2023). Geologically mapped fault traces are available from https://esdynamics.geo.uni-tuebingen.de/faults/ (Mohadjer et al., 2015).

References

An, M. (2012). A simple method for determining the spatial resolution of a general inverse problem. *Geophysical Journal International*, *191*(2), 849–864. https://doi.org/10.1111/j.1365-246x.2012.05661.x

An, Y., Wang, D., Ma, Q., Xu, Y., Li, Y., Zhang, Y., et al. (2022). Preliminary report of the 5 September 2022 MS 6.8 Luding earthquake, Sichuan, China. *Earthquake Research Advances*, *3*(1), 100184. https://doi.org/10.1016/j.eqrea.2022.100184

Antoine, S. L., Klinger, Y., Delorme, A., Wang, K., Bürgmann, R., & Gold, R. D. (2021). Diffuse deformation and surface faulting distribution from submetric image correlation along the 2019 Ridgecrest, California, ruptures. *Bulletin of the Seismological Society of America*, *111*(5), 2275–2302. https://doi.org/10.1785/0120210036

ASF. (2023). Sentinel-1 synthetic aperture radar (SAR) data [Dataset]. Retrieved from https://asf.alaska.edu/data-sets/sar-data-sets/sentinel-1/

Backus, G., & Gilbert, F. (1968). The resolving power of gross earth data. *Geophysical Journal International*, *16*(2), 169–205. https://doi.org/10.1111/j.1365-246x.1968.tb00216.x

Bai, M., Chevalier, M.-L., Pan, J., Replumaz, A., Leloup, P. H., Métois, M., & Li, H. (2018). Southeastward increase of the late Quaternary slip-rate of the Xianshuihe fault, eastern Tibet. Geodynamic and seismic hazard implications. *Earth and Planetary Science Letters*, *485*, 19–31. https://doi.org/10.1016/j.epsl.2017.12.045

Barbot, S., & Fialko, Y. (2010a). Fourier-domain Green's function for an elastic semi-infinite solid under gravity, with applications to earthquake and volcano deformation. *Geophysical Journal International*, *182*(2), 568–582. https://doi.org/10.1111/j.1365-246x.2010.04655.x

Barbot, S., & Fialko, Y. (2010b). A unified continuum representation of post-seismic relaxation mechanisms: Semi-analytic models of afterslip, poroe-lastic rebound and viscoelastic flow. *Geophysical Journal International*, *182*(3), 1124–1140. https://doi.org/10.1111/j.1365-246x.2010.04678.x

Barbot, S., Fialko, Y., & Bock, Y. (2009). Postseismic deformation due to the Mw 6.0 2004 Parkfield earthquake: Stress-driven creep on a fault with spatially variable rate-and-state friction parameters. *Journal of Geophysical Research*, *114*(B7), B07405. https://doi.org/10.1029/2008jb005748

Barbot, S., Fialko, Y., & Sandwell, D. (2008). Effect of a compliant fault zone on the inferred earthquake slip distribution. *Journal of Geophysical Research*, *113*(B6), B06404. https://doi.org/10.1029/2007jb005256

Barbot, S., Fialko, Y., & Sandwell, D. (2009). Three-dimensional models of elasto-static deformation in heterogeneous media, with applications to the Eastern California Shear Zone. *Geophysical Journal International*, *179*(1), 500–520. https://doi.org/10.1111/j.1365-246x.2009.04194.x

Barbot, S., Hamiel, Y., & Fialko, Y. (2008). Space geodetic investigation of the co- and post-seismic deformation due to the 2003 M_w 7.1 Altai earthquake: Implications for the local lithospheric rheology. *Journal of Geophysical Research*, *113*(B3), B03403. https://doi.org/10.1029/2007jb005063

Barker, T. G. (1976). Quasi-static motions near the San Andreas fault zone. *Geophysical Journal International*, *45*(3), 689–705. https://doi.org/10.1111/j.1365-246x.1976.tb06918.x

Barnhart, W., & Lohman, R. (2010). Automated fault model discretization for inversions for coseismic slip distributions. *Journal of Geophysical Research*, *115*(B10), B10419. https://doi.org/10.1029/2010jb007545

Biggs, J., Wright, T., Lu, Z., & Parsons, B. (2007). Multi-interferogram method for measuring interseismic deformation: Denali Fault, Alaska. *Geophysical Journal International*, *170*(3), 1165–1179. https://doi.org/10.1111/j.1365-246x.2007.03415.x

Bürgmann, R., & Dresen, G. (2008). Rheology of the lower crust and upper mantle: Evidence from rock mechanics, geodesy, and field observations. *Annual Review of Earth and Planetary Sciences*, *36*(1), 531–567. https://doi.org/10.1146/annurev.earth.36.031207.124326

Burov, E., & Watts, A. (2006). The long-term strength of continental lithosphere: "jelly sandwich", or "crème brûlée"? *Geological Society of America Today*, *16*(1), 4–10. https://doi.org/10.1130/1052-5173(2006)016<4:tltsoc>2.0.co;2

Clark, M. K., & Royden, L. H. (2000). Topographic ooze: Building the eastern margin of Tibet by lower crustal flow. *Geology*, *28*(8), 703–706. https://doi.org/10.1130/0091-7613(2000)28<703:tobtem>2.0.co;2

Dettmer, J., Benavente, R., Cummins, P. R., & Sambridge, M. (2014). Trans-dimensional finite-fault inversion. *Geophysical Journal International*, *199*(2), 735–751. https://doi.org/10.1093/gji/ggu280

De Zan, F., Zonno, M., & Lopez-Dekker, P. (2015). Phase inconsistencies and multiple scattering in SAR interferometry. *IEEE Transactions on Geoscience and Remote Sensing*, *53*(12), 6608–6616. https://doi.org/10.1109/tgrs.2015.2444431

Dong, D., Fang, P., Bock, Y., Webb, F., Prawirodirdjo, L., Kedar, S., & Jamason, P. (2006). Spatiotemporal filtering using principal component analysis and Karhunen-Loeve expansion approaches for regional GPS network analysis. *Journal of Geophysical Research*, *111*(B3), B03405. https://doi.org/10.1029/2005jb003806

Fan, G.-W., & Lay, T. (2003). Strong Lg attenuation in the Tibetan Plateau. *Bulletin of the Seismological Society of America*, *93*(5), 2264–2272. https://doi.org/10.1785/0120030052

Fang, J., Ou, Q., Wright, T. J., Okuwaki, R., Amey, R. M., Craig, T. J., et al. (2022). Earthquake cycle deformation associated with the 2021 M_w 7.4 Maduo (Eastern Tibet) earthquake: An intrablock rupture event on a slow-slipping fault from Sentinel-1 InSAR and teleseismic data. *Journal of Geophysical Research: Solid Earth*, *127*, e2022JB024268. https://doi.org/10.1029/2022JB024268

Farr, T., & Kobrick, M. (2000). Shuttle radar topography mission produces a wealth of data. *AGU Eos*, *81*(48), 583–585. https://doi.org/10.1029/eo081i048p00583

Fialko, Y. (2004a). Evidence of fluid-filled upper crust from observations of post-seismic deformation due to the 1992 M_w 7.3 Landers earthquake. *Journal of Geophysical Research*, *109*(B8), B08401. https://doi.org/10.1029/2004JB002985

Fialko, Y. (2004b). Probing the mechanical properties of seismically active crust with space geodesy: Study of the co-seismic deformation due to the 1992 M_w 7.3 Landers (southern California) earthquake. *Journal of Geophysical Research*, *109*(B3), B03307. https://doi.org/10.1029/2003JB002756

Fialko, Y. (2021). Estimation of absolute stress in the hypocentral region of the 2019 Ridgecrest, California, earthquakes. *Journal of Geophysical Research: Solid Earth*, *126*(7), e2021JB022000. https://doi.org/10.1029/2021jb022000

Fialko, Y., & Jin, Z. (2021). Simple shear origin of the cross-faults ruptured in the 2019 Ridgecrest earthquake sequence. *Nature Geoscience*, *14*(7), 513–518. https://doi.org/10.1038/s41561-021-00758-5

Fialko, Y., Khazan, Y., & Simons, M. (2001). Deformation due to a pressurized horizontal circular crack in an elastic half-space, with applications to volcano geodesy. *Geophysical Journal International*, *146*(1), 181–190. https://doi.org/10.1046/j.1365-246x.2001.00452.x

Fialko, Y., Rivera, L., & Kanamori, H. (2005). Estimate of differential stress in the upper crust from variations in topography and strike along the San Andreas fault. *Geophysical Journal International*, *160*(2), 527–532. https://doi.org/10.1111/j.1365-246x.2004.02511.x

Fialko, Y., Sandwell, D., Simons, M., & Rosen, P. (2005). Three-dimensional deformation caused by the Bam, Iran, earthquake and the origin of shallow slip deficit. *Nature*, *435*(7040), 295–299. https://doi.org/10.1038/nature03425

Fialko, Y., Simons, M., & Agnew, D. (2001). The complete (3-D) surface displacement field in the epicentral area of the 1999 M_w 7.1 Hector Mine earthquake, southern California, from space geodetic observations. *Geophysical Research Letters*, *28*(16), 3063–3066. https://doi.org/10.1029/2001gl013174

Freed, A. M., & Bürgmann, R. (2004). Evidence of power-law flow in the Mojave desert mantle. *Nature*, *430*(6999), 548–551. https://doi.org/10.1038/nature02784

Freymueller, J., King, N. E., & Segall, P. (1994). The co-seismic slip distribution of the Landers earthquake. *Bulletin of the Seismological Society of America*, *84*(3), 646–659. https://doi.org/10.1785/bssa0840030646

Funning, G. J., Parsons, B., & Wright, T. J. (2007). Fault slip in the 1997 Manyi, Tibet earthquake from linear elastic modelling of InSAR displacements. *Geophysical Journal International*, *169*(3), 988–1008. https://doi.org/10.1111/j.1365-246x.2006.03318.x

Gomba, G., Parizzi, A., De Zan, F., Eineder, M., & Bamler, R. (2015). Toward operational compensation of ionospheric effects in SAR interferograms: The split-spectrum method. *IEEE Transactions on Geoscience and Remote Sensing*, *54*(3), 1446–1461. https://doi.org/10.1109/tgrs.2015.2481079

Gonzalez-Ortega, A., Fialko, Y., Sandwell, D., Alejandro Nava-Pichardo, F., Fletcher, J., Gonzalez-Garcia, J., et al. (2014). El Mayor-Cucapah (M_w 7.2) earthquake: Early near-field postseismic deformation from InSAR and GPS observations. *Journal of Geophysical Research: Solid Earth*, *119*(2), 1482–1497. https://doi.org/10.1002/2013jb010193

Guo, R., Yang, H., Li, Y., Zheng, Y., & Zhang, L. (2022). Complex slip distribution of the 2021 M_w 7.4 Maduo, China, earthquake: An event occurring on the slowly slipping fault. *Seismological Research Letters*, *93*(2A), 653–665. https://doi.org/10.1785/0220210226

Hamiel, Y., & Fialko, Y. (2007). Structure and mechanical properties of faults in the North Anatolian Fault system from InSAR observations of coseismic deformation due to the 1999 Izmit (Turkey) earthquake. *Journal of Geophysical Research*, *112*(B7), B07412. https://doi.org/10.1029/2006jb004777

Hamling, I. J., Hreinsdóttir, S., Clark, K., Elliott, J., Liang, C., Fielding, E., et al. (2017). Complex multifault rupture during the 2016 M_w 7.8 Kaikōura earthquake, New Zealand. *Science*, *356*(6334), eaam7194. https://doi.org/10.1126/science.aam7194

He, K., Wen, Y., Xu, C., & Zhao, Y. (2022). Fault geometry and slip distribution of the 2021 M_w 7.4 Maduo, China, earthquake inferred from InSAR measurements and relocated aftershocks. *Seismological Society of America*, *93*(1), 8–20. https://doi.org/10.1785/0220210204

Hearn, E. H., & Bürgmann, R. (2005). The effect of elastic layering on inversions of GPS data for coseismic slip and resulting stress changes: Strike-slip earthquakes. *Bulletin of the Seismological Society of America*, *95*(5), 1637–1653. https://doi.org/10.1785/0120040158

Henriquet, M., Avouac, J.-P., & Bills, B. G. (2019). Crustal rheology of southern Tibet constrained from lake-induced viscoelastic deformation. *Earth and Planetary Science Letters*, *506*, 308–322. https://doi.org/10.1016/j.epsl.2018.11.014

Herring, T. A., Melbourne, T. I., Murray, M. H., Floyd, M. A., Szeliga, W. M., King, R. W., et al. (2016). Plate boundary observatory and related networks: GPS data analysis methods and geodetic products. *Reviews of Geophysics*, *54*(4), 759–808. https://doi.org/10.1002/2016rg000529

Hsu, Y.-J., Avouac, J.-P., Yu, S.-B., Chang, C.-H., Wu, Y.-M., & Woessner, J. (2009). Spatio-temporal slip, and stress level on the faults within the western foothills of Taiwan: Implications for fault frictional properties. *Pure and Applied Geophysics*, *166*(10), 1853–1884. https://doi.org/10.1007/s00024-009-0510-5

Huang, M.-H., Bürgmann, R., & Freed, A. M. (2014). Probing the lithospheric rheology across the eastern margin of the Tibetan Plateau. *Earth and Planetary Science Letters*, *396*, 88–96. https://doi.org/10.1016/j.epsl.2014.04.003

Jacobs, A., Sandwell, D., Fialko, Y., & Sichoix, L. (2002). The 1999 (M_w 7.1) Hector Mine, California, earthquake: Near-field postseismic deformation from ERS interferometry. *Bulletin of the Seismological Society of America*, *92*(4), 1433–1442. https://doi.org/10.1785/0120000908

Jin, Z., & Fialko, Y. (2020). Finite slip models of the 2019 Ridgecrest earthquake sequence constrained by space geodetic data and aftershock locations. *Bulletin of the Seismological Society of America*, *110*(4), 1660–1679. https://doi.org/10.1785/0120200060

Jin, Z., & Fialko, Y. (2021). Coseismic and early postseismic deformation due to the 2021 M7.4 Maduo (China) earthquake. *Geophysical Research Letters*, *48*(21), e2021GL095213. https://doi.org/10.1029/2021gl095213

Jin, Z., Fialko, Y., Yang, H., & Li, Y. (2023). Transient deformation excited by the 2021 M7.4 Maduo (China) earthquake: Evidence of a deeper shear zone [Dataset]. Zenodo. https://doi.org/10.5281/zenodo.7689859

Jin, Z., Fialko, Y., Zubovich, A., & Schöne, T. (2022). Lithospheric deformation due to the 2015 M7.2 Sarez (Pamir) earthquake constrained by 5 years of space geodetic observations. *Journal of Geophysical Research: Solid Earth*, *127*(4), e2021JB022461. https://doi.org/10.1029/2021jb022461

Jonsson, S., Segall, P., Pedersen, R., & Bjornsson, G. (2003). Post-earthquake ground movements correlated to pore-pressure transients. *Nature*, *424*(6945), 179–183. https://doi.org/10.1038/nature01776

Kaneko, Y., & Fialko, Y. (2011). Shallow slip deficit due to large strike-slip earthquakes in dynamic rupture simulations with elasto-plastic off-fault response. *Geophysical Journal International*, *186*(3), 1389–1403. https://doi.org/10.1111/j.1365-246x.2011.05117.x

Klinger, Y., Xu, X., Tapponnier, P., Van der Woerd, J., Lasserre, C., & King, G. (2005). High-resolution satellite imagery mapping of the surface rupture and slip distribution of the Mw7.8, 14 November 2001 Kokoxili earthquake, Kunlun fault, northern Tibet, China. *Bulletin of the Seismological Society of America*, *95*(5), 1970–1987. https://doi.org/10.1785/0120040233

Lapusta, N., Rice, J., Ben-Zion, Y., & Zheng, G. (2000). Elastodynamic analysis for slow tectonic loading with spontaneous rupture episodes on faults with rate- and state-dependent friction. *Journal of Geophysical Research*, *105*(B10), 23765–23789. https://doi.org/10.1029/2000jb900250

Lau, N., Tymofyeyeva, E., & Fialko, Y. (2018). Variations in the long-term uplift rate due to the Altiplano–Puna magma body observed with Sentinel-1 interferometry. *Earth and Planetary Science Letters*, *491*, 43–47. https://doi.org/10.1016/j.epsl.2018.03.026

Li, Y., Bürgmann, R., & Taira, T. (2023). Spatiotemporal variations of surface deformation, shallow creep rate, and slip partitioning between the San Andreas and southern Calaveras Fault. *Journal of Geophysical Research: Solid Earth*, *128*(1), e2022JB025363. https://doi.org/10.1029/2022jb025363

Lin, G., Shearer, P. M., & Fialko, Y. (2006). Obtaining absolute locations for quarry seismicity using remote sensing data. *Bulletin of the Seismological Society of America*, *96*(2), 722–728. https://doi.org/10.1785/0120050146

Liu, S., Xu, X., Klinger, Y., Nocquet, J.-M., Chen, G., Yu, G., & Jónsson, S. (2019). Lower crustal heterogeneity beneath the northern Tibetan Plateau constrained by GPS measurements following the 2001 M_w 7.8 Kokoxili earthquake. *Journal of Geophysical Research: Solid Earth*, *124*(11), 11992–12022. https://doi.org/10.1029/2019jb017732

Lohman, R. B., & Simons, M. (2005). Some thoughts on the use of InSAR data to constrain models of surface deformation: Noise structure and data downsampling. *Geochemistry, Geophysics, Geosystems*, *6*(1), Q01007. https://doi.org/10.1029/2004gc000841

Marone, C., & Scholz, C. H. (1988). The depth of seismic faulting and the upper transition from stable to unstable slip regimes. *Geophysical Research Letters*, *15*(6), 621–624. https://doi.org/10.1029/gl015i006p00621

McNamara, D., Walter, W., Owens, T., & Ammon, C. (1997). Upper mantle velocity structure beneath the Tibetan Plateau from Pn travel time tomography. *Journal of Geophysical Research*, *102*(B1), 493–505. https://doi.org/10.1029/96jb02112

Meade, B. J. (2007). Algorithms for the calculation of exact displacements, strains, and stresses for triangular dislocation elements in a uniform elastic half space. *Computers & Geosciences*, *33*(8), 1064–1075. https://doi.org/10.1016/j.cageo.2006.12.003

Mitchell, E., Fialko, Y., & Brown, K. M. (2013). Temperature dependence of frictional healing of westerly granite: Experimental observations and numerical simulations. *Geochemistry, Geophysics, Geosystems*, *14*(3), 567–582. https://doi.org/10.1029/2012gc004241

Mitchell, E., Fialko, Y., & Brown, K. M. (2016). Velocity-weakening behavior of Westerly granite at temperature up to 600°C. *Journal of Geophysical Research: Solid Earth*, *121*(9), 6932–6946. https://doi.org/10.1002/2016jb013081

Mohadjer, S., Strube, T., Ehlers, T., & Bendick, R. (2015). Central Asia fault database [Dataset]. Retrieved from https://esdynamics.geo.uni-tuebingen.de/faults/

Ni, J., & Barazangi, M. (1983). High-frequency seismic wave propagation beneath the Indian Shield, Himalayan arc, Tibetan Plateau and surrounding regions: High uppermost mantle velocities and efficient Sn propagation beneath Tibet. *Geophysical Journal International*, *72*(3), 665–689. https://doi.org/10.1111/j.1365-246x.1983.tb02826.x

Okada, Y. (1985). Surface deformation due to shear and tensile faults in a half-space. *Bulletin of the Seismological Society of America*, *75*(4), 1135–1154. https://doi.org/10.1785/bssa0750041135

Pan, J., Li, H., Chevalier, M.-L., Tapponnier, P., Bai, M., Li, C., et al. (2022). Co-seismic rupture of the 2021, M_w 7.4 Maduo earthquake (northern Tibet): Short-cutting of the Kunlun fault big bend. *Earth and Planetary Science Letters*, *594*, 117703. https://doi.org/10.1016/j.epsl.2022.117703

Pearse, J., & Fialko, Y. (2010). Mechanics of active magmatic intraplating in the Rio Grande Rift near Socorro, New Mexico. *Journal of Geophysical Research*, *115*(B7), B07413. https://doi.org/10.1029/2009jb006592

Peltzer, G., Rosen, P., Rogez, F., & Hudnut, K. (1998). Poroelastic rebound along the Landers 1992 earthquake surface rupture. *Journal of Geophysical Research*, *103*(B12), 30131–30145. https://doi.org/10.1029/98jb02302

Perfettini, H., & Avouac, J. (2007). Modeling afterslip and aftershocks following the 1992 Landers earthquake. *Journal of Geophysical Research*, *112*(B7), B07409. https://doi.org/10.1029/2006jb004399

Pollitz, F. F. (2003). Transient rheology of the uppermost mantle beneath the Mojave Desert, California. *Earth and Planetary Science Letters*, *215*(1–2), 89–104. https://doi.org/10.1016/s0012-821x(03)00432-1

Rodgers, A. J., & Schwartz, S. Y. (1998). Lithospheric structure of the Qiangtang Terrane, northern Tibetan Plateau, from complete regional waveform modeling: Evidence for partial melt. *Journal of Geophysical Research*, *103*(B4), 7137–7152. https://doi.org/10.1029/97jb03535

Rosen, P., Hensley, S., Joughin, I., Li, F., Madsen, S., Rodriguez, E., & Goldstein, R. (2000). Synthetic aperture radar interferometry. *Proceedings of the IEEE*, *88*(3), 333–382. https://doi.org/10.1109/5.838084

Roten, D., Olsen, K., & Day, S. (2017). Off-fault deformations and shallow slip deficit from dynamic rupture simulations with fault zone plasticity. *Geophysical Research Letters*, *44*(15), 7733–7742. https://doi.org/10.1002/2017gl074323

Rousset, B., Barbot, S., Avouac, J.-P., & Hsu, Y.-J. (2012). Postseismic deformation following the 1999 Chi-Chi earthquake, Taiwan: Implication for lower-crust rheology. *Journal of Geophysical Research*, *117*(B12), B12405. https://doi.org/10.1029/2012jb009571

Royden, L. H., Burchfiel, B. C., King, R. W., Wang, E., Chen, Z., Shen, F., & Liu, Y. (1997). Surface deformation and lower crustal flow in eastern Tibet. *Science*, *276*(5313), 788–790. https://doi.org/10.1126/science.276.5313.788

Ryder, I., Bürgmann, R., & Pollitz, F. (2011). Lower crustal relaxation beneath the Tibetan Plateau and Qaidam basin following the 2001 Kokoxili earthquake. *Geophysical Journal International*, *187*(2), 613–630. https://doi.org/10.1111/j.1365-246x.2011.05179.x

Sandwell, D., Mellors, R., Tong, X., Wei, M., & Wessel, P. (2011). Open radar interferometry software for mapping surface deformation. *EOS, Transactions American Geophysical Union*, *92*(28), 234. https://doi.org/10.1029/2011eo280002

Savage, J. C. (1990). Equivalent strike-slip earthquake cycles in half-space and lithosphere-asthenosphere earth models. *Journal of Geophysical Research*, *95*(B4), 4873–4879. https://doi.org/10.1029/jb095ib04p04873

Simons, M., Fialko, Y., & Rivera, L. (2002). Coseismic deformation from the 1999 M_w 7.1 Hector Mine, California, earthquake, as inferred from InSAR and GPS observations. *Bulletin of the Seismological Society of America*, *92*(4), 1390–1402. https://doi.org/10.1785/0120000933

Takeuchi, C., & Fialko, Y. (2012). Dynamic models of interseismic deformation and stress transfer from plate motion to continental transform faults. *Journal of Geophysical Research*, *117*(B5), B05403. https://doi.org/10.1029/2011jb009056

Takeuchi, C., & Fialko, Y. (2013). On the effects of thermally weakened ductile shear zones on postseismic deformation. *Journal of Geophysical Research: Solid Earth*, *118*(12), 6295–6310. https://doi.org/10.1002/2013jb010215

Tapponnier, P., Peltzer, G., Le Dain, A., Armijo, R., & Cobbold, P. (1982). Propagating extrusion tectonics in Asia: New insights from simple experiments with plasticine. *Geology*, *10*(12), 611–616. https://doi.org/10.1130/0091-7613(1982)10<611:petian>2.0.co;2

Taylor, M., & Yin, A. (2009). Active structures of the Himalayan-Tibetan orogen and their relationships to earthquake distribution, contemporary strain field, and Cenozoic volcanism. *Geosphere*, *5*(3), 199–214. https://doi.org/10.1130/ges00217.1

Thatcher, W. (2007). Microplate model for the present-day deformation of Tibet. *Journal of Geophysical Research*, *112*(B1), B01401. https://doi.org/10.1029/2005jb004244

Thomas, A. L. (1993). Poly3d: A three-dimensional, polygonal element, displacement discontinuity boundary element computer program with applications to fractures, faults, and cavities in the Earth's crust. Master Thesis at Stanford University.

Tong, X., Sandwell, D., & Fialko, Y. (2010). Coseismic slip model of the 2008 Wenchuan earthquake derived from joint inversion of interferometric synthetic aperture radar, GPS, and field data. *Journal of Geophysical Research*, *115*(B4), B04314. https://doi.org/10.1029/2009jb006625

Toupin, R. A. (1965). Saint-Venant's principle. *Archive for Rational Mechanics and Analysis*, *18*(2), 83–96. https://doi.org/10.1007/bf00282253

Tymofyeyeva, E., & Fialko, Y. (2015). Mitigation of atmospheric phase delays in InSAR data, with application to the Eastern California Shear Zone. *Journal of Geophysical Research: Solid Earth*, *120*(8), 5952–5963. https://doi.org/10.1002/2015jb011886

Tymofyeyeva, E., Fialko, Y., Jiang, J., Xu, X., Sandwell, D., Bilham, R., et al. (2019). Slow slip event on the southern San Andreas fault triggered by the 2017 M_w 8.2 Chiapas (Mexico) earthquake. *Journal of Geophysical Research: Solid Earth*, *124*(9), 9956–9975. https://doi.org/10.1029/2018jb016765

Unsworth, M. (2010). Magnetotelluric studies of active continent–continent collisions. *Surveys in Geophysics*, *31*(2), 137–161. https://doi.org/10.1007/s10712-009-9086-y

Unsworth, M., Wenbo, W., Jones, A. G., Li, S., Bedrosian, P., Booker, J., et al. (2004). Crustal and upper mantle structure of northern Tibet imaged with magnetotelluric data. *Journal of Geophysical Research*, *109*(B2), B02403. https://doi.org/10.1029/2002jb002305

Voronoi, G. (1908). Nouvelles applications des paramètres continus à la théorie des formes quadratiques. deuxième mémoire. recherches sur les parallélloèdres primitifs. *Journal für die Reine und Angewandte Mathematik*, *1908*(134), 198–287. https://doi.org/10.1515/crll.1908.134.198

Wang, K., & Bürgmann, R. (2020). Probing fault frictional properties during afterslip updip and downdip of the 2017 M_w 7.3 Sarpol-e Zahab earthquake with space geodesy. *Journal of Geophysical Research: Solid Earth*, *125*(11), e2020JB020319. https://doi.org/10.1029/2020jb020319

Wang, K., & Fialko, Y. (2014). Space geodetic observations and models of postseismic deformation due to the 2005 M7.6 Kashmir (Pakistan) earthquake. *Journal of Geophysical Research: Solid Earth*, *119*(9), 7306–7318. https://doi.org/10.1002/2014jb011122

Wang, K., & Fialko, Y. (2015). Slip model of the 2015 M_w 7.8 Gorkha (Nepal) earthquake from inversions of ALOS-2 and GPS data. *Geophysical Research Letters*, *42*(18), 7452–7458. https://doi.org/10.1002/2015gl065201

Wang, K., & Fialko, Y. (2018). Observations and modeling of co- and postseismic deformation due to the 2015 M_w 7.8 Gorkha (Nepal) earthquake. *Journal of Geophysical Research: Solid Earth*, *123*(1), 761–779. https://doi.org/10.1002/2017jb014620

Wang, M., Shen, Z.-K., Wang, Y., Bürgmann, R., Wang, F., Zhang, P.-Z., et al. (2021). Postseismic deformation of the 2008 Wenchuan earthquake illuminates lithospheric rheological structure and dynamics of eastern Tibet. *Journal of Geophysical Research: Solid Earth*, *126*(9), e2021JB022399. https://doi.org/10.1029/2021jb022399

Wang, R., Lorenzo-Martin, F., & Roth, F. (2006). PSGRN/PSCMP-a new code for calculating co- and post-seismic deformation, geoid and gravity changes based on the viscoelastic-gravitational dislocation theory. *Computers & Geosciences*, *32*(4), 527–541. https://doi.org/10.1016/j.cageo.2005.08.006

Wang, R., Martin, F., & Roth, F. (2003). Computation of deformation induced by earthquakes in a multi-layered elastic crust - FORTRAN programs EDGRN/EDCMP. *Computers & Geosciences*, *29*(2), 195–207. https://doi.org/10.1016/s0098-3004(02)00111-5

Wang, W., Fang, L., Wu, J., Tu, H., Chen, L., Lai, G., & Zhang, L. (2021). Aftershock sequence relocation of the 2021 Ms7.4 Maduo earthquake, Qinghai, China. *Science China Earth Sciences*, *64*(8), 1371–1380. https://doi.org/10.1007/s11430-021-9803-3

Wei, M., Kaneko, Y., Liu, Y., & McGuire, J. J. (2013). Episodic fault creep events in California controlled by shallow frictional heterogeneity. *Nature Geoscience*, *6*(7), 566–570. https://doi.org/10.1038/ngeo1835

Wei, W., Unsworth, M., Jones, A., Booker, J., Tan, H., Nelson, D., et al. (2001). Detection of widespread fluids in the Tibetan crust by magnetotelluric studies. *Science*, *292*(5517), 716–718. https://doi.org/10.1126/science.1010580

Wessel, P., Smith, W. H., Scharroo, R., Luis, J., & Wobbe, F. (2013). Generic mapping tools: Improved version released. *Eos, Transactions American Geophysical Union*, *94*(45), 409–410. https://doi.org/10.1002/2013eo450001

Wilks, K. R., & Carter, N. L. (1990). Rheology of some continental lower crustal rocks. *Tectonophysics*, *182*(1–2), 57–77. https://doi.org/10.1016/0040-1951(90)90342-6

Wright, T. J., Elliott, J. R., Wang, H., & Ryder, I. (2013). Earthquake cycle deformation and the Moho: Implications for the rheology of continental lithosphere. *Tectonophysics*, *609*, 504–523. https://doi.org/10.1016/j.tecto.2013.07.029

Xiong, X., Shan, B., Zheng, Y., & Wang, R. (2010). Stress transfer and its implication for earthquake hazard on the Kunlun fault, Tibet. *Tectonophysics*, *482*(1–4), 216–225. https://doi.org/10.1016/j.tecto.2009.07.020

Yang, H., Wang, D., Guo, R., Xie, M., Zang, Y., Wang, Y., et al. (2022). Rapid report of the 8 January 2022 MS 6.9 Menyuan earthquake, Qinghai, China. *Earthquake Research Advances*, *2*(1), 100113. https://doi.org/10.1016/j.eqrea.2022.100113

Yue, H., Shen, Z.-K., Zhao, Z., Wang, T., Cao, B., Li, Z., et al. (2022). Rupture process of the 2021 M7.4 Maduo earthquake and implication for deformation mode of the Songpan-Ganzi terrane in Tibetan Plateau. *Proceedings of the National Academy of Sciences of the United States of America*, *119*(23), e2116445119. https://doi.org/10.1073/pnas.2116445119

Zhao, D., Qu, C., Bürgmann, R., Gong, W., & Shan, X. (2021a). Relaxation of Tibetan lower crust and afterslip driven by the 2001 M_w 7.8 Kokoxili, China, earthquake constrained by a decade of geodetic measurements. *Journal of Geophysical Research: Solid Earth*, *126*(4), e2020JB021314. https://doi.org/10.1029/2020jb021314

Zhao, D., Qu, C., Chen, H., Shan, X., Song, X., & Gong, W. (2021b). Tectonic and geometric control on fault kinematics of the 2021 M_w 7.3 Maduo (China) earthquake inferred from interseismic, coseismic, and postseismic InSAR observations. *Geophysical Research Letters*, *48*(18), e2021GL095417. https://doi.org/10.1029/2021gl095417

Zhao, W.-L., & Morgan, W. J. (1987). Injection of Indian crust into Tibetan lower crust: A two-dimensional finite element model study. *Tectonics*, *6*(4), 489–504. https://doi.org/10.1029/tc006i004p00489

Zheng, Y., Fattahi, H., Agram, P., Simons, M., & Rosen, P. (2022). On closure phase and systematic bias in multilooked SAR interferometry. *IEEE Transactions on Geoscience and Remote Sensing*, *60*, 1–11. https://doi.org/10.1109/tgrs.2022.3167648

Zhu, L., & Rivera, L. (2002). A note on the dynamic and static displacements from a point source in multilayered media. *Geophysical Journal International*, *148*(3), 619–627. https://doi.org/10.1046/j.1365-246x.2002.01610.x

Zhu, Y., Diao, F., Fu, Y., Liu, C., & Xiong, X. (2021). Slip rate of the seismogenic fault of the 2021 Maduo earthquake in western China inferred from GPS observations. *Science China Earth Sciences*, *64*(8), 1363–1370. https://doi.org/10.1007/s11430-021-9808-0